


2018

Resonant Anisotropic Emission in RABBITT Spectroscopy

Bejan M. Ghomashi
University of Central Florida

 Part of the [Atomic, Molecular and Optical Physics Commons](#), and the [Quantum Physics Commons](#)
Find similar works at: <https://stars.library.ucf.edu/honorsthesis>
University of Central Florida Libraries <http://library.ucf.edu>

This Open Access is brought to you for free and open access by the UCF Theses and Dissertations at STARS. It has been accepted for inclusion in Honors Undergraduate Theses by an authorized administrator of STARS. For more information, please contact STARS@ucf.edu.

Recommended Citation

Ghomashi, Bejan M., "Resonant Anisotropic Emission in RABBITT Spectroscopy" (2018). *Honors Undergraduate Theses*. 451.
<https://stars.library.ucf.edu/honorsthesis/451>



RESONANT ANISOTROPIC EMISSION IN RABBITT SPECTROSCOPY

by

BEJAN GHOMASHI

A thesis submitted in partial fulfillment of the requirements
for the Honors in the Major Program in Physics
in the College of Sciences
and in the Burnett Honors College
at the University of Central Florida
Orlando, Florida

Summer Term, 2018

Thesis Chair: Luca Argenti, Ph.D.
Co-Chair: Nicolas Douguet, Ph.D.

ABSTRACT

A variant of RABBITT pump-probe spectroscopy in which the attosecond pulse train comprises both even and odd harmonics of the fundamental IR probe frequency is explored to measure time-resolved photoelectron emission in systems that exhibit autoionizing states. It is shown that the group delay of both one-photon and two-photon resonant transitions is directly encoded in the energy-resolved photoelectron anisotropy as a function of the pump-probe time-delay. This principle is illustrated for a 1D model with symmetric zero-range potentials that supports both bound states and shape-resonances. The model is studied using both perturbation theory and solving the time-dependent Schrödinger equation on a grid. Moreover, we study the case of a realistic atomic system, helium. In both cases, we demonstrate faithful reconstruction of the phase information for resonant photoemission.

The content of this thesis has been presented as a poster at The Division of Atomic, Molecular and Optical Physics (DAMOP) annual conference in Ft. Lauderdale, Florida, USA. Additionally, a manuscript is being is being prepared for submission to a scientific journal.

TABLE OF CONTENTS

LIST OF FIGURES	v
LIST OF TABLES	ix
CHAPTER 1 : INTRODUCTION	1
CHAPTER 2 : TIME EVOLUTION	8
CHAPTER 3 : ANALYTICAL MODEL	12
3.1 Bound State	14
3.2 Scattering States.....	15
3.3 Dipole Matrix Elements.....	20
CHAPTER 4 : NUMERICAL MODEL	25
4.1 Numerical Methods	25
4.2 The Potential, Bound-State and Scattering-States	27
4.3 Photoionization	30

CHAPTER 5 : AB-INITIO: HELIUM	39
5.1 Numerical Methods and Theory	39
5.2 Scattering State and Pulse	43
5.3 Photoionization	44
CHAPTER 6 : Conclusion	47
APPENDIX A : SCATTERING STATE PHASES AND NORMALIZATION	49

LIST OF FIGURES

Figure 3.1	Potential (<i>left</i>) and ground state wavefunction (<i>right</i>). Each region between the delta functions is label with a roman numeral I-IV.	12
Figure 3.2	Plotted is the square of the wavefunction, $ \Psi_E(x) ^2$, at selected energies. <i>Left</i> : An example of an odd resonant state, <i>middle</i> : a scattering state of arbitrary energy for comparison, <i>right</i> : an even resonance scattering state.	17
Figure 3.3	A plot of the asymptotic phaseshift ($\phi_e^{IV}(k) + \phi_o^{IV}(k)$) with the background removed. The background goes like $-20\sqrt{2E}$ and is plotted on top of the phaseshift for comparison.	18
Figure 3.4	Plots of the transcendental equations. The intersection points are the resonant energies.	19
Figure 3.5	The square-module of the dipole matrix elements between the bound- and continuum-states of the analytical model. The parameters for the potential are $V_- = 0.5$ au, $V_+ = 2.5$ au, and $a = 10$ au. The peaks are located at energies $E_1 = 0.047$ au, $E_2 = 0.19$ au, $E_3 = 0.43$ au	21

Figure 3.6	The square-module of the dipole matrix elements between two continuum-states of the analytical model. The parameters for the potential are $V_- = 0.5$ au, $V_+ = 2.5$ au, and $a = 10$ au.	23
Figure 4.1	Diagram of the Lorentzian potentials (<i>red</i>) used in the numerical model and the ground state (<i>purple</i>), which has been scaled slightly larger for clarity. In this case $V_+ = 2.5$, $V_- = 0.5$, and $a = 10$ all in atomic units.	27
Figure 4.2	<i>Left</i> : A plot of the bound-state and scattering-state wave functions from the analytical potential. <i>Right</i> : the bound-state and scattering-states corresponding to the numerical potential. The scattering-state of the right selected is an odd resonance at energy $E = 0.194$ au. The parameters for the potential are $V_- = 0.5$ au, $V_+ = 2.5$ au, and $a = 10$ au.	27
Figure 4.3	The summed even and odd phaseshifts (<i>purple</i>) and the background plotted (<i>blue</i>). The phaseshift without the background is shown in <i>green</i>	28
Figure 4.4	The square-module of the dipole transition matrix elements between two continuum-states in the representative numerical model. The parameters for the potential are the same as the analytical model $V_- = 0.5$ au, $V_+ = 2.5$ au, and $a = 10$ au except of course the delta functions are replaced with Lorentzians.	29
Figure 4.5	<i>Left</i> : Fourier transform of the total pulse. <i>Middle</i> : The components of the pulse plotted separately. <i>Right</i> : The total pulse plotted in time.	30
Figure 4.6	An example of the total photoelectron ionization of both the XUV only and XUV+IR. On the <i>left</i> are the intensities of the sideband (top) and resonance (bottom) with	

only the XUV pump pulses while on the *right* are the intensities with XUV pump + IR probe.

The horizontal-axis in all plots represents the photoelectron energy in atomic units. 31

Figure 4.7 Period of IR: $T_{IR} \approx 123$ au. The sharp phaseshift at ~ 0.194 au is indicative of a resonance. The sideband shows the phaseshift modulated by the absorption of an IR photon 35

Figure 4.8 *Left*: A plot of the square-amplitude and phase at the sideband and the resonance. The square-amplitude is not to scale. The jump of π across the resonance is reflected in the phase of the sideband. *Right*: The amplitude at the resonance plotted in the complex plane. 36

Figure 4.9 *Left*: A plot of the square-amplitude and phase at the sideband and and resonance. The square-amplitude is not to scale. The jump of π across the resonance is reflected in the phase of the sideband. *Right*: The amplitude at the resonance plotted in the complex plane. 37

Figure 5.1 A plot of the wavefunction projected onto the S, P, and D scattering states after $\Delta t = 650$ au. The top row of plots is the amplitude squared, which are scaled dramatically for easier visibility, and the bottom row is the phase. Notice the phase increases by π at the resonant energy (~ -0.69 au) in the P symmetry. 43

Figure 5.2 A plot of the asymmetry around the resonance $2s2p$ state ($E_{res} = -0.69$ au) and the sideband approximately $E_{sb} \sim -0.75$ au. The Fourier transform amplitude and phase is shown in the same regions. The phase varies between $-\pi$ (*blue*) and $+\pi$ (*red*). 44

Figure 5.3 The extracted phaseshift at the sideband (left) and $2s2p$ resonance (middle) are shown on top of the respective square-amplitudes (not to scale). At the resonance, the phase-shift jumps by π and when the amplitude crosses a zero there is a discontinuity of π . The

complex amplitude is plotted in the complex-plane on right. The discontinuity occurs as the amplitude crosses the origin. 45

Figure 5.4 The complex amplitude is fit to the Fano profile expression 5.14. The resonance parameters found are: $q \approx -2.5$, $E_{res} \approx -0.691$ au and $\Gamma \approx 0.001418$ au 46

LIST OF TABLES

Table 3.1	Resonance parameters taken from the first eight resonances from the 1D analytical model.	19
Table 4.1	The resonance parameters tabulated by fitting the asymptotic phaseshift.	28

CHAPTER 1

INTRODUCTION

Since its discovery more than a century ago, the photoelectric effect, i.e., the emission of an electron from an atom, molecule or extended target, due to the absorption of ionizing radiation, has played a fundamental role in our understanding of charge-transfer processes in matter. Photoionization often involves the excitation of transiently bound electronic states, which decay by emitting an electron on a time scale as small as a few femtoseconds. Until the end of the 20th century, photoelectron spectroscopies were limited to study photoemission processes in the stationary regime only. During the last two decades, the development of novel sources of sub-femtosecond extreme ultraviolet (XUV) light pulses, however, has opened the way to the time-resolved studies of electronic dynamics in atoms and molecules at its natural timescale [1–4], as well as to explore autoionizing states that are not accessible by mean of the absorption of a single photon.

In particular, Reconstruction of Attosecond Beating by Interference of Two-Photon Transitions (RABBITT) [5–7] is a common technique in which a train of extreme-ultraviolet (XUV) attosecond pulses are used to pump (excite) a sample in tandem with an infrared-pulse used to probe the system. The XUV pulse train is obtained through the process of High-Harmonic Generation (HHG) [8]. In HHG, an intense and short (few tens of a femtosecond) IR-pulse with fundamental frequency ω_{IR} is focused on an active medium, typically a rare gas atom. At the peaks of the IR

pulse, the field is sufficiently strong to extract an electron from the target via a tunneling effect. The freed electron is subsequently driven by the IR pulse in an oscillatory excursion during which it acquires kinetic energy tens or even hundreds of times larger than the fundamental IR frequency. If, in its motion, the electron collides with the parent ion, it can recombine with it liberating the excess energy (the kinetic energy of the electron plus the ionization potential of the atom) by means of an isolated emission of ultraviolet radiation with a duration of a few hundreds or even less than a hundred attoseconds [9]. One attosecond pulse is released for each maximum, i.e., at every half-cycle of the IR field. As a result, the spectrum of the XUV train is normally comprised of odd multiples of the fundamental IR frequency [10]. It is also possible to add to the IR pulse a small second-harmonic component, which can suppress the peak of the field in one direction and enhance the field in the opposite direction. In this case, the generation of attosecond pulses occurs predominantly each whole IR cycle, and the pulse train then comprises both even and odd multiples of the fundamental frequency [11, 12].

HHG in solids presents another possible source of high energy attosecond pulses. It has been demonstrated that crystal structures maintaining inversion symmetry can produce odd-order harmonics such as fused silica while anisotropic crystals, lacking inversion symmetry, can produce both even and odd harmonics [13, 14]. According to You *et al.* [15], "Solid-state HHG has the potential for high efficiency and high stability because of the use of high-density and rigid target as interaction medium" which may provide an advantage in an experimental setup. Additionally, their results show even and odd harmonics produced at energies as high as 24 eV.

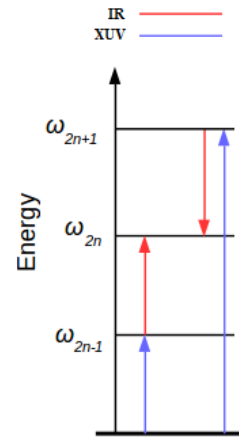
The XUV pulse trains obtained with the HHG processes described above are generally weak (less than 10^{10} W/cm² on focus), and hence they can only be used to promote the absorption of a single harmonic XUV-photon by a target atom or molecule. When used in isolation, a pump attosecond pulse train ionizes the target giving rise to a photoelectron spectrum featuring sharp peaks in correspondence with the harmonics of the fundamental IR frequency. If the ionization takes place in the presence of a weak probe replica of the initial IR pulse, with a controllable delay with respect to the XUV train, however, new multi-photon ionization paths become possible [7]. Besides the absorption of single XUV harmonics, the most relevant paths leading to ionization entail again the absorption of an XUV-photon, accompanied by the exchange (either emission or absorption) of an IR-photon.

Let us consider the traditional case in which the XUV train spectrum comprises only odd harmonics of the fundamental IR frequency.

In this case, the photoelectron spectrum exhibits harmonic sidebands, corresponding to the absorption of an even multiple $2n$ of IR quanta of energy, that can be reached either by absorption of an XUV-photon from the $2n - 1$ odd harmonic, followed by the absorption of an IR photon, or by absorption of an XUV-photon from the consecutive $2n + 1$ odd harmonic, followed by the stimulated emission of an

IR photon. The image on the right is a diagram representing the transitions to continuum-states accessible in traditional RABBITT.

Traditional RABBITT



Thanks to the inherent coherence between the XUV and IR pulses, the amplitudes $\mathcal{A}_{2n-1,\ell}^{(+)}$ and $\mathcal{A}_{2n+1,\ell}^{(-)}$ associated with these two ionization paths and a photoelectron of angular momentum ℓ interfere: the total sideband photoionization probability I_{2n} is proportional to the square of the sum of the two amplitudes,

$$I_{2n} \propto \sum_l \left| \mathcal{A}_{2n-1,\ell}^{(+)} + \mathcal{A}_{2n+1,\ell}^{(-)} \right|^2 = \sum_l \left\{ \left| \mathcal{A}_{2n-1,\ell}^{(+)} \right|^2 + \left| \mathcal{A}_{2n+1,\ell}^{(-)} \right|^2 + 2\Re e \left[\mathcal{A}_{2n-1,\ell}^{* (+)} \mathcal{A}_{2n+1,\ell}^{(-)} \right] \right\}.$$

Due to the interference term and the fact that the amplitude $\mathcal{A}_{2n\pm 1,\ell}^{(\mp)}$ comprises the term $e^{\pm i\omega\tau}$, the sideband signal oscillates at twice the fundamental IR frequency, $I_{2n} \propto \cos(2\omega\tau + \phi_{2n})$ [16, 17], where τ is the pump-probe time delay and ϕ_{2n} is a phase shift characteristic of the sideband. Indeed, the $\mathcal{A}_{2n\pm 1,\ell}^{(\mp)}$ amplitudes depend on the central position of the IR pulse as $e^{\pm i\omega\tau}$.

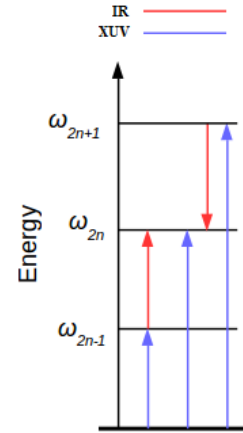
The phase shift ϕ_{2n} are particularly important since they incorporate information about both the relative phase of two consecutive harmonics (e.g., due to a chirp in the XUV pulse train) and the additional "atomic" phase acquired by the photoelectron in the photoemission process itself. In the special case in which one of the two harmonics excites a resonant state, the other harmonic can act as a holographic reference. The phaseshift in the sideband beating as a function of the detuning of the first harmonic from the intermediate resonance, therefore, exhibits the rapid excursion characteristic of resonant amplitudes. From such a profile, it is possible to reconstruct in time the fast process with which the metastable state gives rise to the resonant feature in the photoelectron spectrum as it decays to the continuum. If the two harmonics excite two different resonances, then the RABBITT beating can in principle be used to reconstruct the fast dynamics of the coherent metastable wavepacket thus generated. Conversely, several closely spaced intermediate states

can be excited by the same harmonics, in which case the integral RABBITT sideband signal will exhibit frequency components shifted by the beating frequency between resonant components.

In the RABBITT set up examined above, for spherically symmetric targets, such as closed-shell atoms, both harmonic and sideband photoelectron amplitudes have definite parity with respect to inversion (odd and even, respectively, corresponding to the parity number of exchanged photons). As a consequence, the photoelectron distributions are symmetric with respect to inversion along the plane perpendicular to the polarization axis of the external pulses.

Checkerboard RABBITT

In the case the XUV spectrum comprises both even and odd harmonics of the IR frequency (attosecond pulses separated by a whole IR period), the effect of the IR probe pulse is quite different from the one described above. The reason is that at all the photoelectron energies the dominant ionization amplitude is the one associated with the absorption of a single XUV harmonic, \mathcal{A}_n . The IR pulse promotes an additional exchange of an IR photon, so that, to lowest order, the angle-resolved ionization probability at the position of the n^{th} harmonics is,



$$\sigma_n \propto \sum_{\ell} \left| \mathcal{A}_{n,\ell} + \mathcal{A}_{n-1,\ell\pm 1}^{(+)} + \mathcal{A}_{n+1,\ell\pm 1}^{(-)} \right|^2 \approx \sum_{\ell} \left\{ |\mathcal{A}_{n,\ell}|^2 + 2\Re \left[\mathcal{A}_{n,\ell}^* \left(\mathcal{A}_{n-1,\ell\pm 1}^{(+)} + \mathcal{A}_{n+1,\ell\pm 1}^{(-)} \right) \right] \right\}.$$

In contrast to the previous case, the beating results from the interference between one-photon and two-photon transition paths. The amplitude of the beating is proportional to the variation with the energy of the peak harmonic intensity of the XUV spectrum and to the *amplitude* (rather than to the intensity) of the IR probe pulse. Furthermore, the beating distribution has odd parity,

since it originates from the interference between odd and even amplitudes (one- and two-photon amplitudes, respectively). This means that the beating contrast is visible only in the angularly resolved detections (e.g., upward vs downward photoemission).

Apart from the measurement peculiarities of the method, which may represent an advantage or not, depending on the detector used (e.g.: magnetic bottle [18], time-of-flight directional detector [19, 20], velocity-map-imaging [21, 22], or COLTRIMS [23, 24]) this approach presents some conceptual advantages over the traditional RABBITT for the reconstruction of photoelectron wave packets because of the two-photon arm can be unstructured and serve as a reference, whereas the resonant amplitude can be a pure one-photon transition. This means that the one-photon resonant amplitude, and hence the resonant photoemission group delay associated with it [25], can be obtained directly, instead of being inferred from the two-photon transition amplitude, which requires one to make *ad hoc* assumptions to disentangle the on-shell sequential one-photon and the virtual components.

This thesis has the following outline. In chapter 2 we summarize the time-dependent theory that is needed to describe time-resolved single-ionization photoelectron emission processes from the simple atomic system, in particular, helium, both in terms of lowest-order perturbation theory and in terms of the direct solution of the time-dependent Schrödinger equation. In chapter 3 we illustrate a 1D model that supports transiently bound states and which we can use to illustrate the method. We describe the bound and scattering states of the system, as well as the dipole transition matrix elements between them, computed analytically. This matrix is used to compute the one-photon and two-photon transition amplitudes, and therefore the asymmetry of the photoionization.

Chapter 4 will discuss the model system in which the results of interacting with the laser field will be found by numerically solving the time-dependent Schrödinger equation. The bound and free states are computed along with the transition matrix elements and photoionization spectrum which are compared with the analytical model. In chapter 5 we consider a full-fledged B-spline closed-coupling numerical representation of the helium atom, in the electrostatic approximation, which accurately reproduces the electronic continuum of the atom in the single-ionization energy region. In particular, we will focus on the region between the first and second excitation threshold of the He^+ parent ion, whose time-resolved dynamics has not been explored yet.

CHAPTER 2

TIME EVOLUTION

The time evolution of a quantum system is governed by the time-dependent Schrödinger equation (TDSE),

$$i\hbar \frac{\partial \Psi(t)}{\partial t} = H\Psi(t)$$

where $\Psi(t)$ is the wavefunction describing the state of the system, and H is the total Hamiltonian. The Hamiltonian comprises of the time-independent potential V of the field-free system as well as the interaction with the laser pulse and kinetic energy. For one electron,

$$H = \frac{(\vec{P} + \alpha \vec{A}(t))^2}{2m} + V = \frac{1}{2m} (P^2 + \alpha^2 A^2(t) + 2\alpha \vec{A} \cdot \vec{P}) + V$$

where $A(t)$ is the vector potential of the external field, $\alpha = e^2/\hbar c \approx 1/137.035$ is the fine-structure constant, \vec{P} is the canonical momentum and m is the electron mass. In the dipole approximation, the term quadratic in A is a global time-dependent constant which can be eliminated by means of a unitary transformation. For moderately intense fields, even beyond the dipole approximation, the non-uniform component of the quadratic term is negligible with respect to the linear term and therefore can be neglected.

$$H = \frac{P^2}{2m} + V(x) + \frac{\alpha \vec{A} \cdot \vec{P}}{m}$$

The TDSE can be solved numerically or by using time-dependent perturbation theory if the pulse is sufficiently weak, which is the case for two-photon RABBITT spectroscopy.

To express the perturbative solution, it is convenient to reformulate the TDSE in interaction representation and in integral form. To do so, the field-free Hamiltonian H_0 is separated from the time-dependent interaction term $H'(t)$

$$H(t) = H_0 + H'(t)$$

$$H_0 = \frac{P^2}{2m} + V(x) \quad \text{and} \quad H'(t) = \frac{\alpha A(t) \mathcal{O}}{m} = \frac{\alpha \vec{A}(t) \cdot \vec{P}}{m}.$$

It is convenient to incorporate the field polarization in the dipole operator,

$$\vec{A}(t) = A(t) \hat{\epsilon}, \quad \mathcal{O} \equiv \hat{\epsilon} \cdot \vec{P}.$$

In the interaction picture,

$$\Psi_I(t) = e^{iH_0 t} \Psi(t) \quad \text{and} \quad H'_I(t) = e^{iH_0 t} H'(t) e^{-iH_0 t}$$

and the Schrödinger equation can be cast in the integral form

$$\Psi_I(t) = \Psi_I(t_0) - i \int_{t_0}^t dt' H'_I(t') \Psi_I(t'). \quad (2.1)$$

Recursively substituting the equation into the integral, one can define a series expansion for the unitary time evolution operator to an arbitrary order,

$$\Psi_I(t) = U(t, t_0) \Psi_I(t_0), \quad U(t, t_0) = \sum_{m=0}^{\infty} U^{(m)}(t, t_0) \quad (2.2)$$

$$U^{(0)}(t, t_0) = 1 \quad (2.3)$$

$$U^{(m)}(t, t_0) = \frac{1}{i\hbar} \int_{t_0}^t dt_1 \int_{t_0}^{t_1} dt_2 \dots \int_{t_0}^{t_{m-1}} dt_m H'_I(t_1) H'_I(t_2) \dots H'_I(t_m) \quad (2.4)$$

We can then define the correction to the wavefunction to m-th order as

$$\Psi^{(m)}(t) \equiv U^{(m)}(t, t_0) \Psi(t_0)$$

If the system is initially in the ground state $|g\rangle$, the probability $\mathcal{A}_{E \leftarrow g}$ of finding the system in a final state $|E\rangle$, with total energy E , at any time t after the end of the pulses is

$$\mathcal{A}_{E \leftarrow g} = \sum_m \mathcal{A}_{E \leftarrow g}^{(m)}, \quad \mathcal{A}_{E \leftarrow g}^{(m)} = \langle E_I | \Psi_I^{(m)}(t) \rangle$$

In particular, the first- and second-order terms are:

$$\begin{aligned} \mathcal{A}_{E \leftarrow g}^{(0)} &= \langle E_I | g_I \rangle = 0 \\ \mathcal{A}_{E \leftarrow g}^{(1)}(t) &= -\frac{i}{\hbar} \int_{t_0}^t dt' \langle E_I | H_I'(t') | g_I \rangle \\ &= -\frac{i}{\hbar} \alpha \langle E | \mathcal{O} | g \rangle \int_{t_0}^t dt' A(t') e^{-(E_g - E)t'/\hbar} \\ \mathcal{A}_{E \leftarrow g}^{(2)}(t) &= \left(\frac{1}{i\hbar} \right)^2 \alpha^2 \sum_m \langle E | \mathcal{O} | m \rangle \langle m | \mathcal{O} | g \rangle \times \\ &\quad \int_{t_0}^t dt' \int_{t_0}^{t'} dt'' A(t') e^{-i(E_m - E)t'/\hbar} A(t'') e^{-i(E_g - E_m)t''/\hbar} \end{aligned}$$

The equations can also be represented in the frequency domain [17]

$$\mathcal{A}_{E \leftarrow g}^{(1)}(\omega) = -\frac{i}{\hbar} \alpha \langle E | \mathcal{O} | g \rangle \tilde{F}(\omega_{Eg}) \quad (2.5)$$

$$\mathcal{A}_{E \leftarrow g}^{(2)}(\omega) = -i\alpha^2 \int_{-\infty}^{\infty} d\omega \tilde{F}(\omega_{Eg} - \omega) \tilde{F}(\omega) \mathcal{M}_{(E \leftarrow g)}^{(2)} \quad (2.6)$$

$$\mathcal{M}_{(E \leftarrow g)}^{(2)} = \langle E | \mathcal{O} G_0^+(E_g + \omega) \mathcal{O} | g \rangle \quad (2.7)$$

where $\tilde{F}(\omega) = 1/\sqrt{2\pi} \int dt A(t) e^{-i\omega t}$ is the Fourier transform of the field amplitude, $G_0^+ = (E - H_0 + i0^+)^{-1}$ is the retarded resolvent of the field-free Hamiltonian and $\omega_{Eg} = (E - E_g)/\hbar$.

If we are able to compute the one- and two-photon dipole matrix elements between arbitrary states of the system we can also compute the ionization probability that results from the interaction between the system, initially in the bound state, with an arbitrary sequence of weak pulses, under the assumption that all terms beyond second order are negligible.

CHAPTER 3

ANALYTICAL MODEL

In this chapter, we consider a simple 1D analytical model given by a bound electron in interaction with a potential comprising three delta functions. As we will see, such a model can be parameterized to give rise to bound as well as autoionizing states. Furthermore, its solutions have a simple analytic expression. The potential comprises two repulsive delta functions of magnitude V_+ located at $\pm a$ on the x-axis and a single attractive potential at the origin of magnitude V_- .

The field-free Hamiltonian H_0 and the potential V are,

$$H_0 = \frac{P^2}{2} + V(x)$$

$$V(x) = V_+ \delta(x-a) + V_+ \delta(x+a) - V_- \delta(x)$$

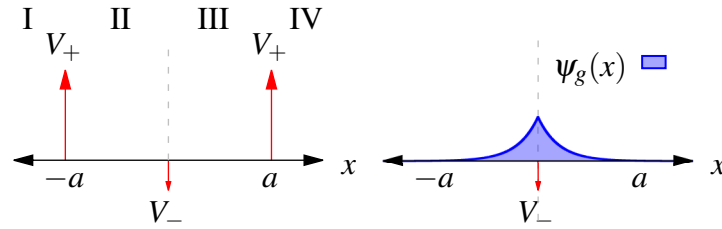


Figure 3.1: Potential (*left*) and ground state wavefunction (*right*). Each region between the delta functions is label with a roman numeral I-IV.

where $P = -i\frac{d}{dx}$. Here and in the following we will assume atomic units ($m_e = 1, q_e = 1, \hbar = 1$) unless otherwise stated.

The stationary states are found by solving the time-independent Schrödinger equation,

$$H_o \psi(x) = E \psi(x), \quad \psi \in \mathcal{L}^2(\mathbb{R}).$$

Solutions of the Schrödinger equation must be continuous and, wherever the potentials are finite, the solutions are differentiable as well, whereas at the points where the potential diverges (impenetrable barriers and delta potentials) the wave function can be discontinuous in its first spatial derivative. The magnitude of this discontinuity can be calculated by integrating the Schrödinger equation around the delta function of magnitude α located at x_0 .

$$\begin{aligned} 0 &= \lim_{\varepsilon \rightarrow 0} \int_{x_0 - \varepsilon}^{x_0 + \varepsilon} \left[-\frac{1}{2} \frac{d^2 \psi(x)}{dx^2} - (E - \alpha \delta(x - x_0)) \psi(x) \right] dx \\ &= -\frac{1}{2} \left[\psi'(x)|_{x=x_0^+} - \psi'(x)|_{x=x_0^-} \right] + \alpha \psi(0) \end{aligned}$$

The result of which reveals the following boundary conditions:

$$\psi(x)|_{x=x_0^+} = \psi(x)|_{x=x_0^-} \tag{3.1}$$

$$\psi'(x)|_{x=x_0^+} = \psi'(x)|_{x=x_0^-} \pm 2\alpha \psi(x)|_{x=x_0}. \tag{3.2}$$

in the region between two consecutive deltas of the potential, where the Hamiltonian is reduced to that of a free particle, a general solution $\psi(x)$ with energy E is.

$$\psi(x) = Ae^{\kappa x} + Be^{-\kappa x}, \quad \kappa = \sqrt{-2E} \quad E < 0,$$

$$\psi(x) = Ae^{ikx} + Be^{-ikx}, \quad k = \sqrt{2E} \quad E > 0$$

3.1 Bound State

Thanks to the presence of the central attractive component of the potential at the origin, the system supports one (and only one) bound state, i.e., an eigenfunction with negative energy and which is normalizable. For a single attractive delta potential, the wavefunctions must exponentially decrease away from the origin to remain normalizable. This condition eliminates term that increases exponentially for $x \rightarrow \pm\infty$,

$$\psi^I(x) = A_g e^{\kappa x} \quad \text{when } x \leq 0 \quad (3.3)$$

$$\psi^{II}(x) = A_g e^{-\kappa x} \quad \text{when } x \geq 0 \quad (3.4)$$

The normalization constants and the energy of the bound state can be calculated easily by imposing the first boundary condition, Eq. (3.1), upon the wavefunctions at the location of the delta potential, $x_0 = 0$.

$$\begin{aligned} 0 &= \psi(x)|_{x=0^+} - \psi(x)|_{x=0^-} \\ &= -\frac{1}{2}[-\kappa - \kappa] - V_- \\ \kappa &= V_- \end{aligned} \quad (3.5)$$

and the normalization:

$$\begin{aligned} 1 &= 2A_g^2 \int_0^\infty e^{-2\kappa x} dx \\ &= \frac{A_g^2}{\kappa} \\ A_g &= \sqrt{V_-} \end{aligned} \quad (3.6)$$

The repulsive potentials will also cause a discontinuity in the first derivative of the wave function proportional to the wavefunction at their respective locations which can be seen in the boundary conditions (Eq. (3.2)). If the repulsive potentials are far away enough from the origin or, conversely, the attractive potential is sufficiently strong, the wavefunction of the bound state at $|x| \geq a$ is negligible, and because the discontinuity caused by the delta function is proportional to the wavefunction at that location the discontinuity is also negligible. In Figure 3.1 we show the profile of the bound state wave function for $a = 10$ au and $V_- = 0.5$ au. As it is clear from the figure, for a range of parameters of the binding potentials, the wavefunction is negligible at the confining potentials, therefore the bound state is unaffected at $x = \pm a$.

3.2 Scattering States

The scattering states can be solved for by taking advantage of the symmetry of the potential. In contrast with the bound state, for each positive energy there are two independent solutions to the secular problem. Because the potential V is symmetric, however, the parity operator Π commutes with the field-free Hamiltonian,

$$\Pi|x\rangle = |-x\rangle, \quad [H_0, \Pi] = 0$$

As a consequence, the eigenstates of H_0 can be constructed to be eigenstates of Π as well, i.e., to be either even or odd under the inversion of the spatial coordinate. In the following, we will label the coefficients, phases, and other attributes of the even and odd functions with the e and o subscript, respectively.

The even and odd functions at energy $E = k^2/2 > 0$ have the following asymptotic ($|x| > a$) form,

$$\psi_o(x) = A_o(k) \sin[kx + \phi_o(k)] \quad (3.7)$$

$$\psi_e(x) = A_e(k) \sin[kx + \phi_e(k)] \quad (3.8)$$

Notice how, due to their symmetry, the amplitude and phase shift of both even and odd functions needs to be specified only in the positive x -direction. The corresponding values for negative x are automatically determined.

Continuum wave functions generally have different phase and amplitude in two consecutive regions. The change of both phases and amplitudes, however, are determined by the boundary conditions. The phases and amplitude as a function of the energy are as follows in S.I. units

$$\phi_o^{IV}(k) = \operatorname{arccot} \left[\cot(ka) + \frac{2m}{k\hbar^2} V_+ \right] - ka \quad \text{Odd phase, region IV}$$

$$\phi_e^{III}(k) = \arctan \left[\frac{k\hbar^2}{mV_-} \right] \quad \text{Even phase, region III}$$

$$\phi_e^{IV}(k) = \operatorname{arccot} \left\{ \cot[ka + \phi_e^{III}(k)] + \frac{2m}{k\hbar^2} V_+ \right\} - ka \quad \text{Even phase, region IV}$$

$$[A_o^{IV}]^2 = 1 + \left[\frac{2m}{k\hbar^2} V_+ \sin(ka) \right]^2 + \frac{2m}{k\hbar^2} V_+ \sin(2ka)$$

$$[A_e^{IV}]^2 = 1 + \left[\frac{2m}{k\hbar^2} V_+ \sin(ka + \phi_e^{III}(k)) \right]^2 + \frac{2m}{k\hbar^2} V_+ \sin[2ka + \sin(ka + 2\phi_e^{III}(k))]$$

see Appendix A for a full derivation.

The two repulsive potentials have a dramatic effect on the continuum as they can keep the electron outside or confine it inside the barrier. This property is illustrated in Figure 3.2, which shows

Examples of Resonance States

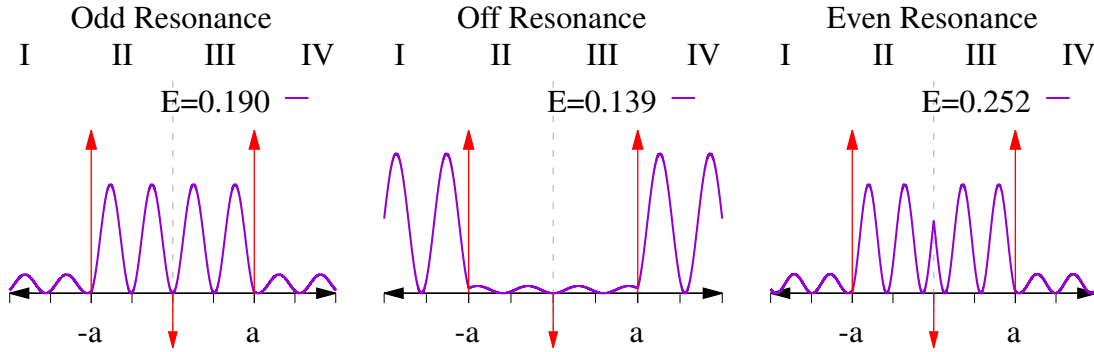


Figure 3.2: Plotted is the square of the wavefunction, $|\Psi_E(x)|^2$, at selected energies. *Left:* An example of an odd resonant state, *middle:* a scattering state of arbitrary energy for comparison, *right:* an even resonance scattering state.

two examples of continuum states. Confined states (left and right of Figure 3.2) indicate that the potential can transiently bind an electron, which would complete tunneling out of the potential only after bouncing back and forth between the barriers multiple times. The confinement mechanism that gives rise to the resonance observed here is the same as in the Fabry-Perót interferometer used in classical optics.

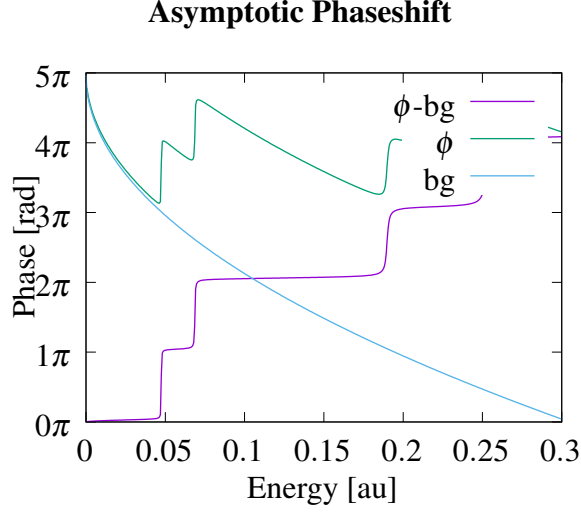


Figure 3.3: A plot of the asymptotic phaseshift ($\phi_e^{IV}(k) + \phi_o^{IV}(k)$) with the background removed. The background goes like $-20\sqrt{2E}$ and is plotted on top of the phaseshift for comparison.

The asymptotic phase also contains dynamical information about the system. Jumps of π reveal the energies corresponding to resonant states and the derivative of this phase with respect to energy is proportional to the time gained or lost due to the potential with respect to a free-particle not interacting with any potential. There is a strong background associated with the potential due to the repulsive delta functions being displaced from the origin. The background goes like $-2ka$ and is subtracted so as to only expose the important features of the phaseshift. To find the resonant energies we look for the points halfway up the jump in the phase, $\frac{\pi}{2}$ (ignoring the background). This corresponds to the argument of $\text{acot}(x)$ being equal to zero, see Eq. (3.9).

$$\begin{aligned} \text{acot}\left(\cot(k_o a) + \frac{2V_+}{k_o}\right) &= \frac{\pi}{2} \quad \rightarrow \quad -\cot(k_o a) = \frac{2V_+}{k_o} \\ \text{acot}\left(\cot(k_e a + \phi_e^{III}) + \frac{2V_+}{k_e}\right) &= \frac{\pi}{2} \quad \rightarrow \quad -\cot(k_e a + \phi_e^{III}) = \frac{2V_+}{k_e} \end{aligned} \quad (3.9)$$

Solutions to these transcendental equations are found by plotting both sides and finding the intersection points. Several of the resonant energies and the parameters are tabulated below.

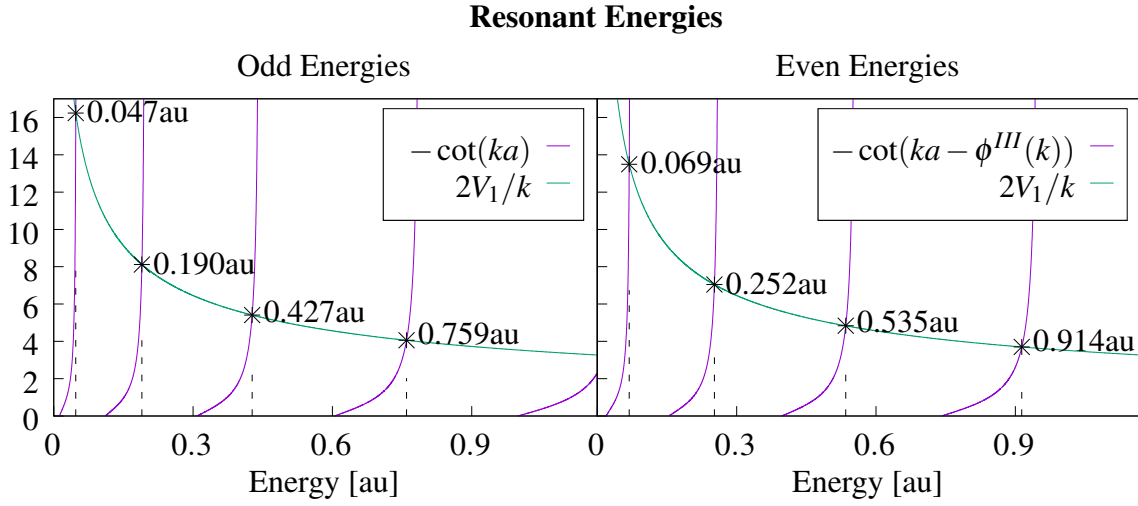


Figure 3.4: Plots of the transcendental equations. The intersection points are the resonant energies.

Energy [au]	Γ [au]	$\hat{\Pi}$
0.047434	0.00023	odd
0.068649	0.00046	even
0.189764	0.00176	odd
0.252001	0.00283	even

Energy [au]	Γ [au]	$\hat{\Pi}$
0.427069	0.00518	odd
0.534709	0.00741	even
0.759490	0.01174	odd
0.913797	0.01613	even

Table 3.1: Resonance parameters taken from the first eight resonances from the 1D analytical model.

3.3 Dipole Matrix Elements

To evaluate the interaction of a charged particle in the model potential with an external time-dependent electric field, we must evaluate the dipole matrix for both bound-continuum and continuum-continuum transitions. Because the ground state is the only bound state and has even parity, bound-continuum transitions only occur to odd states. The matrix elements were found by evaluating the following equation where $|g\rangle$ is the ground state and $|E\rangle$ is an arbitrary odd continuum-state (using atomic units).

$$\mu_{E,g} = \langle E|\hat{p}|g\rangle = -i \int_{-\infty}^{\infty} dx \psi_o^*(x) \frac{d}{dx} \psi_g(x).$$

Under the assumption that the ground-state wavefunction is negligible beyond $x = \pm a$, the dipole integral can be evaluated using the analytical expression for both the initial and final wavefunctions in the inner region only, and extending the integral over $x = [0, \infty]$ (in the following, $E = k^2/2$, $E_g = -\kappa^2/2$ and $A_o^{III} = (A_o^{IV})^{-1}$ normalizing the outer regions to 1),

$$\begin{aligned} \mu_{E,g} &= -2i \int_0^{\infty} dx \psi_o^{*III}(x) \frac{d}{dx} \psi_g(x) \\ &= 2i\kappa A_o^{III} A_g \int_0^{\infty} dx \sin(k_E x) e^{-\kappa x} \\ &= \kappa A_o^{III} A_g \int_0^{\infty} dx e^{-(\kappa - ik_E)x} - e^{-(\kappa + ik_E)x} \\ &= -\frac{\kappa A_o^{III} A_g}{\kappa^2 + k_E^2} [\kappa - ik_E - \kappa - ik_E] \\ \mu_{E,g} &= \frac{2i\kappa k_E A_o^{III} A_g}{\kappa^2 + k_E^2} = \frac{2iA_o^{III} A_g \sqrt{E_g E}}{E_g + E} \end{aligned} \tag{3.10}$$

Figure 3.5 shows the square-module of the bound-continuum dipole matrix element, as a function of the energy of the electron in the final state. The spectrum features several peaks in correspondence with the odd resonant states supported by the potential.

Ground-Continuum Dipole Matrix Elements

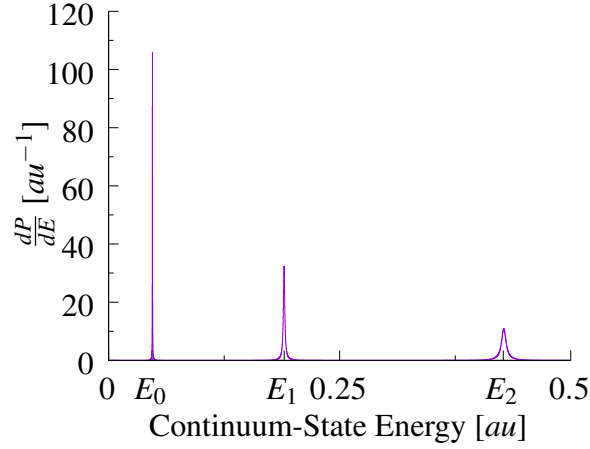


Figure 3.5: The square-module of the dipole matrix elements between the bound- and continuum-states of the analytical model. The parameters for the potential are $V_- = 0.5$ au, $V_+ = 2.5$ au, and $a = 10$ au. The peaks are located at energies $E_1 = 0.047$ au, $E_2 = 0.19$ au, $E_3 = 0.43$ au

The continuum-continuum dipole matrix is less obvious to compute since neither the bra nor the ket is normalizable. As a result, we must expect the appearance of distribution terms. On the other hand, we can use the fact that the bra and ket are eigenfunctions of the field-free Hamiltonian $H_0 = p^2/2 + \sum_i V_i \delta(x - x_i)$, to find an expression for the regular part of the matrix element ($\Psi_{o,E}$ is an odd continuum-state of arbitrary energy E and $\Psi_{e,E'}$ is an even continuum-state of arbitrary

energy E').

$$\begin{aligned}\langle \Psi_{e,E} | \frac{d}{dx} | \Psi_{o,E'} \rangle &= \frac{\mathcal{P}}{E' - E} \langle \Psi_{e,E} | \left[\frac{d}{dx}, H_0 \right] | \Psi_{o,E'} \rangle \\ &\quad + \pi \delta(k - k') \sin[\phi_e(k) - \phi_o(k)] A_e(k) A_o(k)\end{aligned}$$

$$\begin{aligned}\langle \Psi_{e,E} | \left[\frac{d}{dx}, H_0 \right] | \Psi_{o,E'} \rangle &= \sum_i V_i \langle \Psi_{e,E} | \left[\frac{d}{dx}, \delta(x - x_i) \right] | \Psi_{o,E'} \rangle \\ &= \sum_i V_i \left[\frac{d}{dx} \Psi_{e,E}(x) \Psi_{o,E'}(x) \right]_{|x=x_i}\end{aligned}$$

The regular part of the dipole matrix element ($E' \neq E$) is given explicitly by

$$\begin{aligned}\langle \Psi_{e,E} | \frac{d}{dx} | \Psi_{o,E'} \rangle &= (E' - E)^{-1} \left(\right. \\ &\quad \frac{1}{2} [\Psi_o^{II'}(-a) + \Psi_o^{III'}(-a)] \Psi_e^{II}(-a) + \frac{1}{2} [\Psi_e^{II'}(-a) + \Psi_e^{III'}(-a)] \Psi_o^{II}(-a) + \\ &\quad \frac{1}{2} [\Psi_e^{III'}(0) + \Psi_e^{IV'}(0)] \Psi_o^{III}(0) + \frac{1}{2} [\Psi_o^{III'}(0) + \Psi_o^{IV'}(0)] \Psi_e^{III}(0) + \\ &\quad \left. \frac{1}{2} [\Psi_e^{III'}(a) + \Psi_e^{IV'}(a)] \Psi_o^{IV}(a) + \frac{1}{2} [\Psi_o^{III'}(a) + \Psi_o^{IV'}(a)] \Psi_e^{IV}(a) \right)\end{aligned}$$

Taking advantage of the fact that the bra and ket functions have opposite parity

$$\begin{aligned}\langle \Psi_{e,E} | \frac{d}{dx} | \Psi_{o,E} \rangle &= \frac{\Psi_o^{III'}(0) \Psi_e^{III}(0) + [\Psi_o^{IV'}(a) + \Psi_o^{III'}(a)] \Psi_e^{III}(a) + [\Psi_e^{IV'}(a) + \Psi_e^{III'}(a)] \Psi_o^{III}(a)}{E' - E} \\ &= (E' - E)^{-1} \{ k_o [\cos(k_o a + \phi_o^{IV}) + A_o \cos(k_o a)] A_e \sin(k_e + \phi_e^{III}) + \\ &\quad k_e [\cos(k_e a + \phi_e^{IV}) + A_e \cos(k_e a + \phi_e^{III})] A_o \sin(k_o a) + A_o A_e k_o \sin(\phi_e^{III}) \}\end{aligned}$$

The regular part of the continuum-continuum dipole matrix is plotted in Figure 3.6.

Continuum-Continuum Dipole Matrix Elements

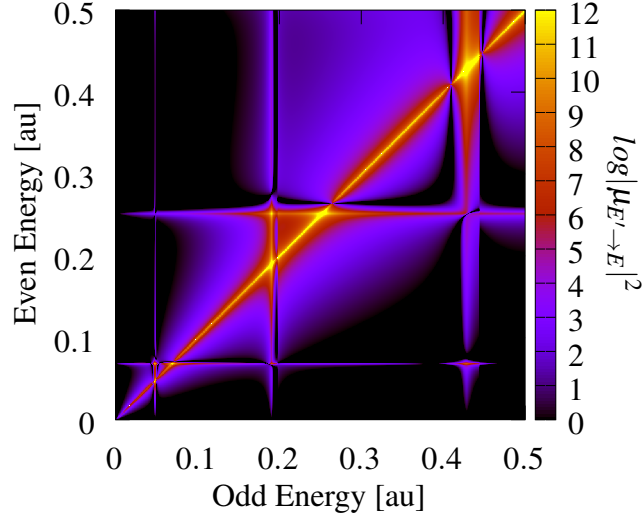


Figure 3.6: The square-module of the dipole matrix elements between two continuum-states of the analytical model. The parameters for the potential are $V_- = 0.5$ au, $V_+ = 2.5$ au, and $a = 10$ au.

At this point, the ground-continuum and continuum-continuum the two-photon transition matrix elements can be calculated using the one-photon dipole elements,

$$\mathcal{M}_{E \leftarrow g}^{(1)} = \langle E | \mathcal{O} | g \rangle \quad (3.11)$$

$$\mathcal{M}_{E \leftarrow g}^{(2)} = \langle E | \mathcal{O} G_0^+ (E_g + \omega) \mathcal{O} | g \rangle. \quad (3.12)$$

$$\begin{aligned} \mathcal{M}_{E \leftarrow g}^{(2)}(\omega) &= \langle E | \mathcal{O} G_0^+ (\omega_g + \omega) \mathcal{O} | g \rangle \\ &= - \sum_{\beta} \int d\varepsilon \frac{\langle E | \frac{d}{dx} | \varepsilon \rangle \langle \varepsilon | \frac{d}{dx} | g \rangle}{\omega_g + \omega - \varepsilon + i0^+} \end{aligned}$$

$$\begin{aligned}
\langle \Psi_{e,E} | \frac{d}{dx} | \Psi_{o,\varepsilon} \rangle \langle \Psi_{o,\varepsilon} | \frac{d}{dx} | g \rangle &= \frac{2\kappa k_o A_o^{III} A_G}{\kappa^2 + k_o^2} \times \frac{2}{k_o^2 - k_e^2} \{ \\
&k_o [\cos(k_o a + \phi_o^{IV}) + A_o \cos(k_o a)] A_e \sin(k_e + \phi_e^{III}) \\
&k_e [\cos(k_e a + \phi_e^{III}) + A_e \cos(k_e a + \phi_e^{IV})] A_o \sin(k_o a) \\
&+ A_o A_e k_o \sin(\phi_e^{III}) \}
\end{aligned}$$

These transition matrices can be used to solve the finite-pulse multi-photon integrals to determine the one- and two-photon perturbative ionization amplitudes (Eq. (2.5) and (2.6)) and the photoionization asymmetry.

CHAPTER 4

NUMERICAL MODEL

A custom one-dimensional solver is developed in-house by N. Douguet and with it, we numerically simulate the time evolution of the wavefunction under the influence of combinations of XUV-pump and IR-probe pulses using the Crank-Nicolson method and the Thomas algorithm. The scattering-states are computed using the Numerov method [26, 27]. After the pulses have passed we project the wavefunction onto the scattering-states in order to retrieve the photoionization spectrum. Because we are interested in this modified RABBITT technique, we analyze the asymmetry in the emission (wavepackets moving left vs wavepackets moving right).

4.1 Numerical Methods

The Numerov method is used to compute the scattering-states and the ground state. In particular it is used to solve equations of the form:

$$\frac{d^2y}{dx^2} = -a(x)y(x) + b(x) \quad or \quad -\frac{d^2\psi}{dx^2} = (E - V(x))\psi(x) \quad (4.1)$$

and solutions can be found by the following discretized equation:

$$\psi_{n+1} \left(1 + \frac{\Delta x^2}{12} (E - V_{n+1}) \right) - 2\psi_n \left(1 - \frac{5\Delta x^2}{12} (E - V_n) \right) + \psi_{n-1} \left(1 + \frac{\Delta x^2}{12} (E - V_{n-1}) \right) = 0 \quad (4.2)$$

To simulate the time evolution the Crank-Nicolson method is used to solve partial differential equations first-order in time and second-order in space. The method is unconditionally stable for equations of the form:

$$\frac{\partial \Psi}{\partial t} = \vec{\nabla}^2 \Psi + V(x, t) \Psi. \quad (4.3)$$

The finite-difference discretization of the Hamiltonian acting on Ψ is:

$$H\Psi \approx -\frac{1}{2\Delta x^2} [\Psi_{i+1} - 2\Psi_i + \Psi_{i-1}] + V_i \Psi_i \quad (4.4)$$

$$\left(1 + \frac{i\Delta t H}{2}\right) \Psi^{n+1} = \left(1 - \frac{i\Delta t H}{2}\right) \Psi^n \quad (4.5)$$

Substituting in $H\Psi$ into equation 4.5:

$$\begin{aligned} -\frac{i\Delta t}{4\Delta x^2} [\Psi_{i+1}^{n+1} + \Psi_{i-1}^{n+1}] + \left(1 + \frac{i\Delta t}{2\Delta x^2} + \frac{i\Delta t}{2} V_i\right) \Psi_i^{n+1} = \\ \frac{i\Delta t}{4\Delta x^2} [\Psi_{i+1}^n + \Psi_{i-1}^n] + \left(1 - \frac{i\Delta t}{2\Delta x^2} - \frac{i\Delta t}{2} V_i\right) \Psi_i^n. \end{aligned} \quad (4.6)$$

Which can be written as a tridiagonal matrix equation.

$$A\Psi^{n+1} = A^*\Psi^n \quad A = \begin{pmatrix} b & a & 0 & \cdots & 0 \\ a & b & a & \cdots & 0 \\ 0 & a & b & \cdots & 0 \\ \vdots & \vdots & \vdots & \ddots & \vdots \\ 0 & 0 & \cdots & a & b \end{pmatrix}, \quad (4.7)$$

$$a = -\frac{i\Delta t}{4\Delta x^2}, \quad b = 1 + \frac{i\Delta t}{2} \left(\frac{1}{\Delta x^2} + V_i \right)$$

This equation is solved at every time-step using Thomas' algorithm [28].

4.2 The Potential, Bound-State and Scattering-States

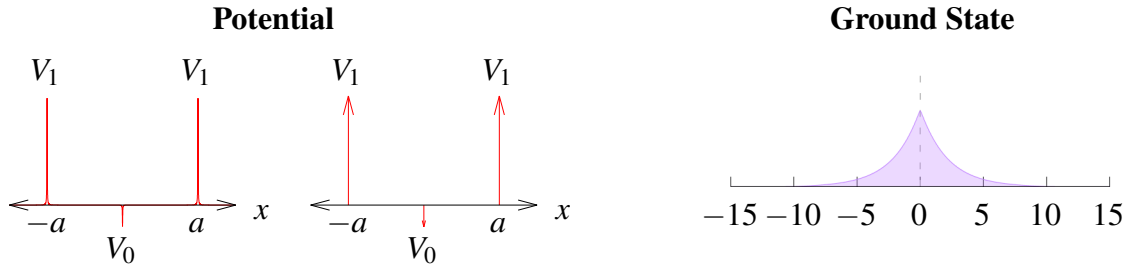


Figure 4.1: Diagram of the Lorentzian potentials (*red*) used in the numerical model and the ground state (*purple*), which has been scaled slightly larger for clarity. In this case $V_+ = 2.5$, $V_- = 0.5$, and $a = 10$ all in atomic units.

When defining the potential, Lorentzian functions are used in place of the delta functions because the numerical solver requires the use of a continuous potential. The Lorentzian potentials are narrowed as tightly as possible while still maintaining the stability of the simulation, $V\delta(x-x_0) \approx V\frac{1}{\pi}\frac{\Gamma/2}{(x-x_0)^2+(\Gamma/2)^2}$. The scattering states are computed and compared to the analytical model with great agreement. In figure 4.2 the bound-state and continuum-states from the analytical and numerical model are plotted on top of their respective potentials.

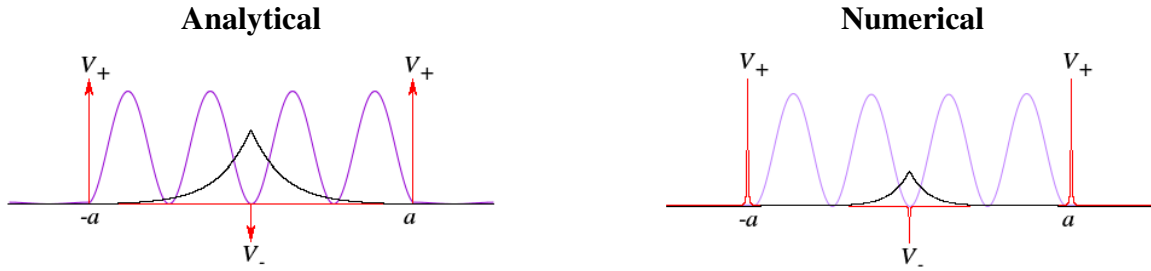


Figure 4.2: *Left:* A plot of the bound-state and scattering-state wave functions from the analytical potential. *Right:* the bound-state and scattering-states corresponding to the numerical potential. The scattering-state of the right selected is an odd resonance at energy $E = 0.194$ au. The parameters for the potential are $V_- = 0.5$ au, $V_+ = 2.5$ au, and $a = 10$ au.

Additionally, the asymptotic phaseshift is computed and, just as the analytical phaseshift, maintains a sharp background that is proportional to $2\sqrt{E}$. The background is computed by fitting the preceding expression (multiplied by a constant) to the phaseshift in the range $E = [0, 0.04]$ where there is only a background. This term is then removed in order to compare the numerical phaseshift with the analytical model in figure 3.3. Furthermore, resonant states are illuminated by jumps of π in the phaseshift as their associated energy is crossed. The first few resonance parameters are found and tabulated in figure (4.3) by fitting $\arctan(\frac{2}{\Gamma}(E - E_{res}))$ to the phaseshift around the energy.

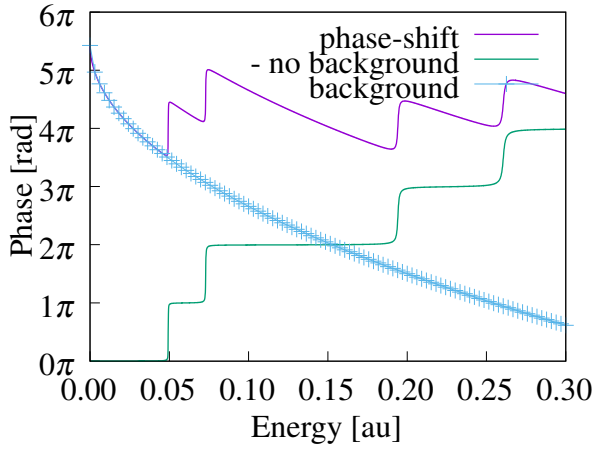


Figure 4.3: The summed even and odd phaseshifts (*purple*) and the background plotted (*blue*). The phase-shift without the background is shown in *green*.

Energy [au]	Γ [au]	$\hat{\Pi}$
0.049309	0.00013	odd
0.072935	0.00029	even
0.194155	0.00118	odd
0.260609	0.00200	even

Table 4.1: The resonance parameters tabulated by fitting the asymptotic phaseshift.

The dipole matrix elements are also computed numerically and compared with the analytical model. The strong agreement between the dipole elements, the phaseshift, and the scattering states gives confidence that the numerical model will exhibit the same properties as the analytical model.

Continuum-Continuum Dipole Matrix Elements

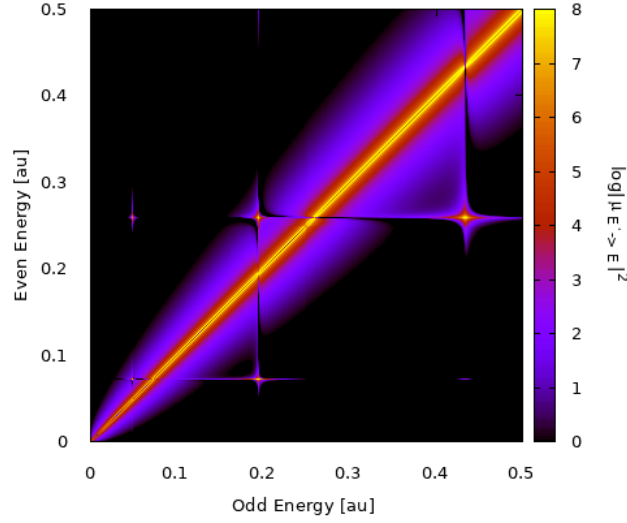


Figure 4.4: The square-module of the dipole matrix elements between two continuum-states in the representative numerical model. The parameters for the potential are the same as the analytical model $V_- = 0.5$ au, $V_+ = 2.5$ au, and $a = 10$ au except of course the delta functions are replaced with Lorentzians.

Finally, the asymptotic phaseshift is used to select a resonant state to populate with the XUV pulses. In particular, the state $E_{res} \approx 0.194$ au is the chosen target and $E \approx 0.137$ au is the state used as a reference in which the one-photon and two-photon transition paths can interfere.

4.3 Photoionization

Example Pulse

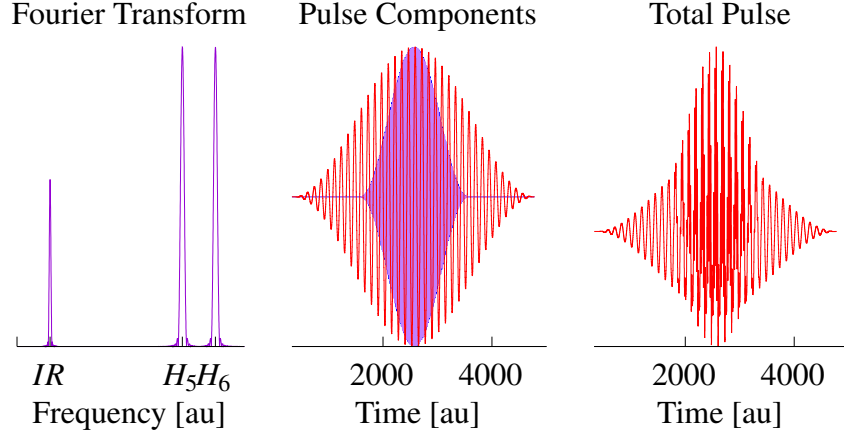


Figure 4.5: *Left:* Fourier transform of the total pulse. *Middle:* The components of the pulse plotted separately. *Right:* The total pulse plotted in time.

In order to simplify the results of the simulation two Gaussian XUV harmonics are used in place of a full APT which allows the states which are stimulated by the pulse to be controlled more finely. This simplification can be justified by considering that the APT can be decomposed into an infinite number of monochromatic XUV pulses each of some intensity. A 32 cycle long IR pulse with frequency $\omega_{IR} = 0.05092$ au (895 nm) is used as the probe pulse while the fifth and sixth harmonics ($\omega_5 \approx 0.2546$ au and $\omega_6 \approx 0.3055$ au) make up the pump. We retrieve the photoelectron spectrum at the end of the simulation of several different time delays between the pump and the probe pulses.

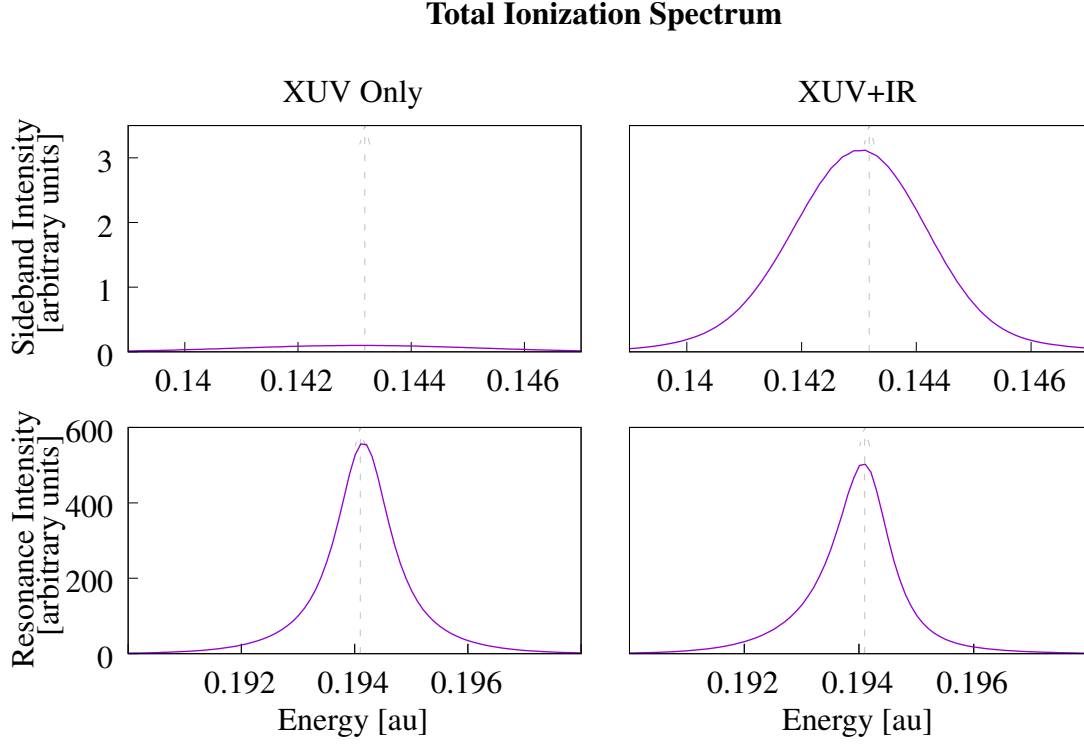


Figure 4.6: An example of the total photoelectron ionization of both the XUV only and XUV+IR. On the *left* are the intensities of the sideband (top) and resonance (bottom) with only the XUV pump pulses while on the *right* are the intensities with XUV pump + IR probe. The horizontal-axis in all plots represents the photoelectron energy in atomic units.

Figure 4.6 shows an example of the total photoelectron distribution after interacting with the laser field. The left column is the ionization intensity at the sideband (top) and target resonance (bottom) energies with only the XUV pump pulses while the right column shows the same photoelectron energy ranges (sideband, resonance) but the laser field includes the XUV and IR pulses. When including the IR pulse the sideband has a significantly increased intensity, by almost a factor of 10, which is indicative of the emission of a photon from an electron occupying the upper har-

monic. The resonance intensity on the other hand largely maintains its magnitude with or without the addition of the IR pulse. This gives us confidence that we are working within the perturbative energy regime.

The photoionization is calculated by projecting the final wave function $\Psi(x)$ after interacting with the laser field on to the energy normalized left-, $\psi_L(x)$, or right-moving, $\psi_R(x)$, scattering states, with asymptotic incoming wave condition from the right or from the left, respectively. These scatterings states are calculated using the Numerov method. Projecting the final wave function on the asymptotic scattering states allows to compute the amplitude as a function of the photoelectron energy:

$$\mathcal{A}_L(E) = \langle \psi_L | \Psi \rangle \quad \text{and} \quad \mathcal{A}_R(E) = \langle \psi_R | \Psi \rangle. \quad (4.8)$$

Where $|\psi_L\rangle$ and $|\psi_R\rangle$ are states in which the outgoing electron is leaving only to the left or right, respectively.

$$\psi_L(x) = \begin{cases} e^{-ikx} + ae^{ikx} & x \leq -a \\ be^{-ikx} & x \geq a \end{cases} \quad \text{and} \quad \psi_R(x) = \begin{cases} de^{ikx} & x \leq -a \\ fe^{-ikx} + e^{ikx} & x \geq a \end{cases}. \quad (4.9)$$

Where,

$$|a|^2 + |b|^2 = 1 \quad \text{and} \quad |d|^2 + |f|^2 = 1 \quad (4.10)$$

Once again, the potential is symmetric and therefore supports states of definite parity so the left- and right-moving scattering states can be written as a superposition of even and odd wavefunctions ψ_e and ψ_o , respectively.

$$|\psi_L\rangle = \frac{1}{\sqrt{2}} [|\psi_e\rangle - |\psi_o\rangle] \quad \text{and} \quad |\psi_R\rangle = \frac{1}{\sqrt{2}} [|\psi_e\rangle + |\psi_o\rangle], \quad (4.11)$$

and therefore,

$$\mathcal{A}_L(E) = \frac{1}{\sqrt{2}} [\langle \psi_e | \Psi \rangle - \langle \psi_o | \Psi \rangle] \quad \text{and} \quad \mathcal{A}_R(E) = \frac{1}{\sqrt{2}} [\langle \psi_e | \Psi \rangle + \langle \psi_o | \Psi \rangle] \quad (4.12)$$

or

$$\mathcal{A}_L(E) = \frac{1}{\sqrt{2}} [\mathcal{A}_e(E) - \mathcal{A}_o(E)] \quad \text{and} \quad \mathcal{A}_R(E) = \frac{1}{\sqrt{2}} [\mathcal{A}_e(E) + \mathcal{A}_o(E)]. \quad (4.13)$$

Using the example pulse above there are two possible transition paths to the energy state corresponding to the absorption of the 6th harmonic, E_6 . One by the absorption of a single XUV photon, H_6 , and another by absorbing an XUV photon, H_5 , and absorbing an IR photon. Because of the definite parity of the states, the one-photon transition brings the electron to an odd state with amplitude $\mathcal{A}_{o,6}$ and the amplitude carries with it the phase of the scattering state. The two-photon path to an even final state, $\mathcal{A}_{e,5}^{(+)}$, carries not only the phase of the one-photon transition through the state corresponding to the absorption of the H_5 harmonic but also acquires a phase $e^{-i\omega_{IR}\tau}$ from the absorption of an IR-photon. It is also possible for the amplitudes to pick up the phase difference between the two harmonics but the phase difference of this example pulse is set to zero. The probability \mathcal{P}_{E_6} for an electron to be found with energy associated with the 6th harmonic and to be on the right is (ignoring the factor of $1/\sqrt{2}$ for clarity),

$$\mathcal{P}_{E_6,R} = |\mathcal{A}_{e,5}^{(+)} + \mathcal{A}_{o,6}|^2 = |\mathcal{A}_{e,5}^{(+)}|^2 + |\mathcal{A}_{o,6}|^2 + 2\Re \left\{ \mathcal{A}_{e,5}^{(+)} \mathcal{A}_{o,6}^* \right\} \quad (4.14)$$

and on the left,

$$\mathcal{P}_{E_6,L} = |\mathcal{A}_{e,5}^{(+)} - \mathcal{A}_{o,6}|^2 = |\mathcal{A}_{e,5}^{(+)}|^2 + |\mathcal{A}_{o,6}|^2 - 2\Re \left\{ \mathcal{A}_{e,5}^{(+)} \mathcal{A}_{o,6}^* \right\}. \quad (4.15)$$

The ω_{IR} beating is not present in the total ionization, $\mathcal{P}_{E_6,L} + \mathcal{P}_{E_6,R}$, because the cross terms cancel. On the other hand, when looking at the asymmetry, $\mathcal{P}_{E_6,L} - \mathcal{P}_{E_6,R}$, the oscillations is what

remains.

$$\mathcal{P}_{E_6,L} - \mathcal{P}_{E_6,R} = -4\Re\left\{\mathcal{A}_{e,5}^{(+)}\mathcal{A}_{o,6}^*\right\} \quad (4.16)$$

$$= -4|\mathcal{A}_{e,5}^{(+)}||\mathcal{A}_{o,6}|\Re\left\{e^{-i(\omega_{IR}\tau+\Delta\phi)}\right\} \quad (4.17)$$

which goes like:

$$\mathcal{P}_{L-R} \propto \cos(\omega_{IR}\tau + \Delta\phi) \quad \Delta\phi = \phi_6 - \phi_5 \quad (4.18)$$

In fact, if the higher harmonic, H_6 , lands on a resonant energy state and the sideband, H_5 , has a negligible phaseshift, $\Delta\phi \rightarrow \phi_6$ the beating in the asymmetry carries the one-photon phaseshift of that resonant state. Analysis of the sideband is essentially the same except the two-photon pathway leads first to the resonance then an IR-photon is emitted in order to reach the sideband.

$$\mathcal{P}_L - \mathcal{P}_R = -4\Re\left\{\mathcal{A}_{o,5}\mathcal{A}_{e,6}^{(-)*}\right\} \quad (4.19)$$

$$= -4|\mathcal{A}_{o,5}||\mathcal{A}_{e,6}^{(-)}|\Re\left\{e^{-i(\omega_{IR}\tau+\Delta\phi)}\right\} \quad (4.20)$$

This modulates the resonance phase carried to the sideband by the emission of the IR-photon.

Therefore, the photoionization asymmetry is found by subtracting the photoelectron distribution to the right from the left at each time delay. In figure 4.7 the asymmetry is plotted as a function of the time delay between the pump and probe pulse demonstrating the predicted ω_{IR} oscillations at the target resonance and sideband. Additionally displayed in figure 4.7 is the Fourier transform which computed at each energy in order to extract the phase and amplitude of the beating.

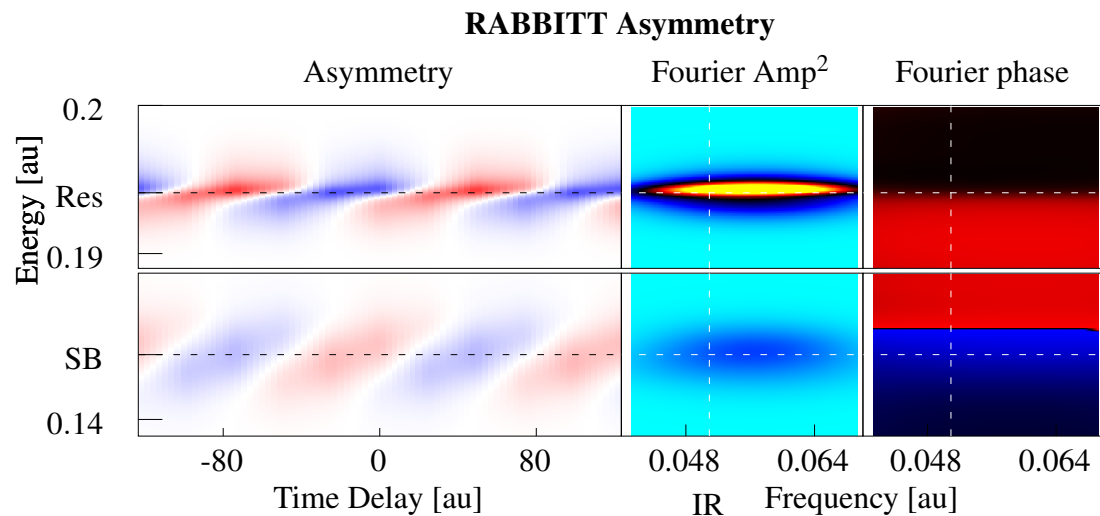


Figure 4.7: Period of IR: $T_{IR} \approx 123$ au. The sharp phaseshift at ~ 0.194 au is indicative of a resonance. The sideband shows the phaseshift modulated by the absorption of an IR photon

The oscillation experiences a dramatic phaseshift across the resonance. In order to extract the phase of the beating the Fourier transform is integrated across a small region around ω_{IR} (the peaks). The result is displayed below.

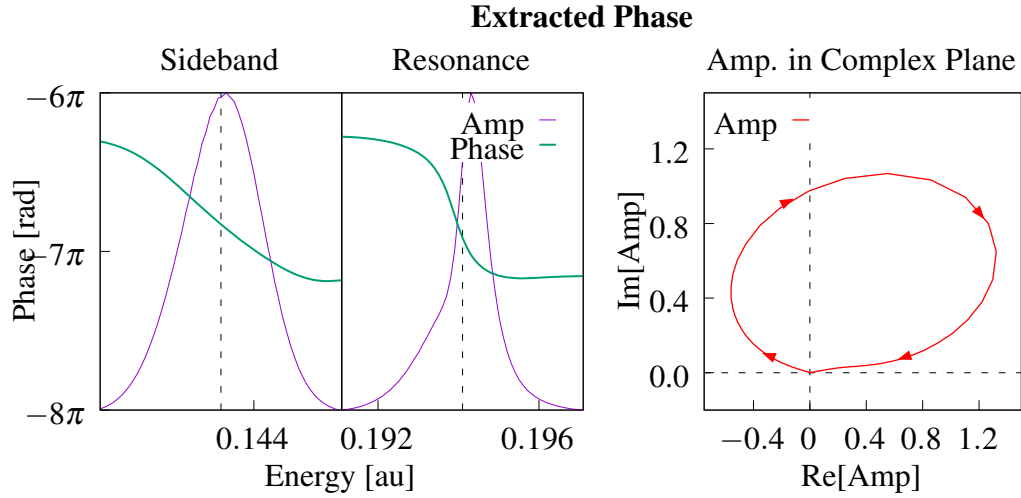


Figure 4.8: *Left:* A plot of the square-amplitude and phase at the sideband and the resonance. The square-amplitude is not to scale. The jump of π across the resonance is reflected in the phase of the sideband. *Right:* The amplitude at the resonance plotted in the complex plane.

The phase is only meaningful in the regions with nonzero amplitude and so only those energies around the sideband and resonant state are shown. The resonant phase exhibits the characteristic jump of π as the energy crosses the resonance and at the sideband the jump of π is modulated by the emission (or absorption) of an IR photon from a pulse of finite width.

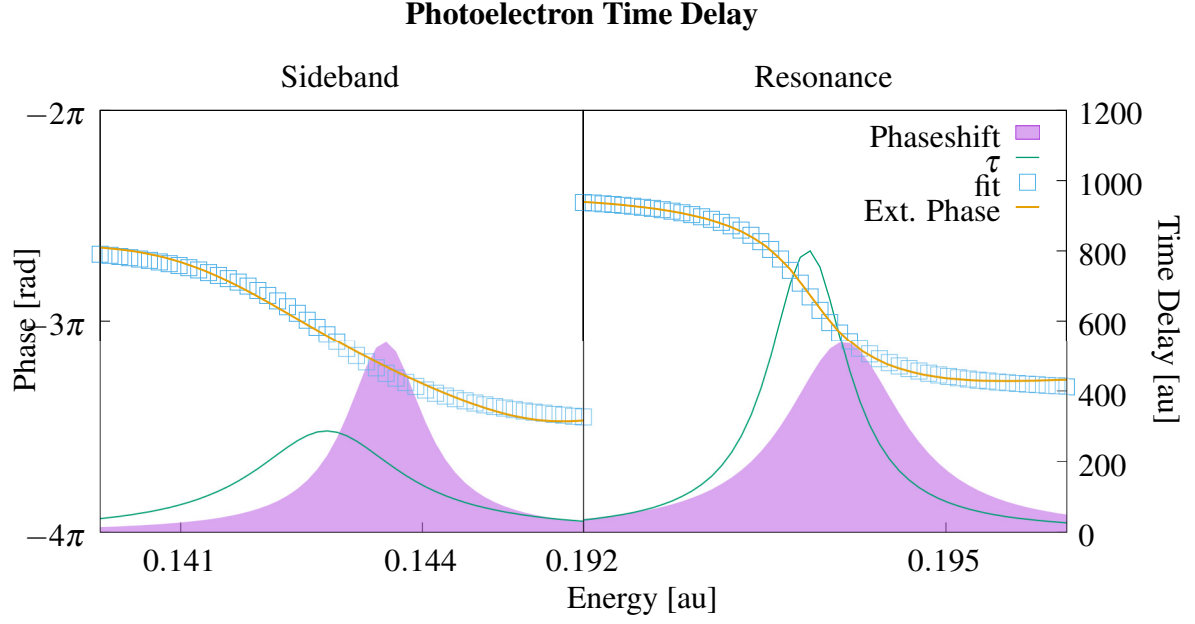


Figure 4.9: *Left:* A plot of the square-amplitude and phase at the sideband and and resonance. The square-amplitude is not to scale. The jump of π across the resonance is reflected in the phase of the sideband.

Right: The amplitude at the resonance plotted in the complex plane.

In order to extract the resonance parameters $\arctan\left(\frac{2}{\Gamma}(E - E_r)\right)$ is fit to the phaseshift at the resonance and at the sideband. In figure 4.9 the fitting is shown in blue, the extracted phase from the simulation in gold. Plotted in green is the derivative of this phase (a Lorentzian) which is the time delay associated with the photoelectron of some energy interacting with the potential. In solid purple, the original resonance parameters from the asymptotic phaseshift (see figure 4.3) are plotted for comparison. The resonance width extract from the fit is $\Gamma \approx 0.0008$ au and the location $E_r = 0.194$ au which are reasonably accurate when compared the parameters taken from the asymptotic phase. It is possible that some of the discrepancies can be accounted for by more careful examination of the effects of the pulse envelope and phase difference between the harmonics.

Additionally, the small shift of the position of the resonance is most likely due to a non-negligible energy dependence of the continuum-continuum phase acquired during the transition from the 5th harmonic to the 6th harmonic.

CHAPTER 5

AB-INITIO: HELIUM

Finally, the same technique is applied to atomic helium. Helium is chosen because it is the smallest neutral atom that supports autoionizing states. In the ab-initio method the atomic wavefunction is represented by a B-spline closed-coupling (CC) expansion. The interaction of the ground state of the helium atom with the applied laser field is computed by integrating the TDSE with a second-order exponential-split propagator. The final photoelectron distribution is obtained by projecting the resulting wavepacket on the scattering states, which are computed separately by solving the Lippmann-Schwinger equation in the CC-space.

$$|\psi^\pm\rangle = |\phi\rangle + \frac{V}{E - H_0 + i0^+} |\psi^{(\pm)}\rangle \quad (5.1)$$

5.1 Numerical Methods and Theory

The CC basis comprises a set of channel functions, $\phi_{\alpha E}$, where a state of the He^+ parent ion (e.g., $1s$, $2s$, $2p$, and so forth) is augmented by all the possible states for a second electron with assigned orbital angular momentum ℓ and whose radial part is itself expanded in a numerical basis that spans the interval from the origin to the radius R of a quantization box. Here a B-spline radial

basis is employed [29]. The ion and additional electron are coupled to give rise to a total well defined angular momentum and spin and the wavefunction is antisymmetrized to comply with Pauli's exclusion principle.

$$\Psi(t) = \sum_{\Gamma} \Psi^{\Gamma}(t) \quad \Gamma = (\Pi, L, S, M, \Sigma) \quad (5.2)$$

$$\Psi^{\Gamma}(t) = \sum_i \chi_i^{\Gamma} c_i^{\Gamma}(t) + \sum_{\alpha} \sum_j \int dE \phi_{\alpha E}^{\Gamma} c_{\alpha E}^{\Gamma}(t)$$

The CC basis also comprises an additional set of localized symmetry adapted configurations χ_i^{Γ} that improve the description of the correlated two-electron wave function at short range.

The time evolution is governed by the TDSE,

$$i \frac{\partial \Psi(t)}{\partial t} = H \Psi(t). \quad (5.3)$$

Where the Hamiltonian is comprised of a field-free part, H_0 and a time-dependent part, $H_I(t)$. H_0 consists of the kinetic energy of both electrons, the attraction of each electron to the nucleus and the electron repulsion term, whereas the time-dependent interaction term, $H_I(t)$ contains the laser field interaction.

$$H = H_0 + H_I(t) \quad (5.4)$$

$$H_0 = \frac{P_1^2}{2} + \frac{P_2^2}{2} - \frac{1}{r_1} - \frac{1}{r_2} + \frac{1}{|r_1 - r_2|} \quad (5.5)$$

$$H_I(t) = \alpha \vec{A}(t) \cdot \vec{P} \quad (5.6)$$

The TDSE is integrated numerically in a sequence of time steps. In each time step the unitary time-evolution propagator is approximated with a second-order split exponential propagator,

$$\Psi(t + dt) = e^{-iH_0 dt/2} e^{-iH_I(t+dt)/2} e^{-iH_0 dt/2} e^{-iV_{caps} dt} \Psi(t) \quad (5.7)$$

where V_{caps} is a complex-absorption potential that prevents reflection of the photoelectrons from the box boundaries.

Because the system is spherically symmetric and the laser pulse is only linearly polarized the angular distribution is azimuthally symmetric and therefore is only dependent upon θ . Written in terms of spherical harmonics, the angular distribution at the n^{th} harmonic is

$$\sigma_n(\theta) \propto \left| \mathcal{A}_{n,p} Y_1^0(\theta) + \left(\mathcal{A}_{n-1,s}^{(+)} + \mathcal{A}_{n+1,s}^{(-)} \right) Y_0^0(\theta) + \left(\mathcal{A}_{n-1,d}^{(+)} + \mathcal{A}_{n+1,d}^{(-)} \right) Y_2^0(\theta) \right|^2, \quad (5.8)$$

or in terms of the Legendre polynomials:

$$\sigma_n(\theta) = \frac{\mathcal{P}_n}{4\pi} [1 + \beta_1 P_1(\cos \theta) + \beta_2 P_2(\cos \theta) + \beta_3 P_3(\cos \theta) + \beta_4 P_4(\cos \theta)]. \quad (5.9)$$

Where \mathcal{P}_n is the total probability of finding an electron with energy associated to the n^{th} harmonic,

$$\mathcal{P}_n = \int \sigma_n d\Omega = |\mathcal{A}_{n,p}|^2 + \sum_{\ell=0,2} \left(\left| \mathcal{A}_{n+1,\ell}^{(-)} \right|^2 + \left| \mathcal{A}_{n-1,\ell}^{(+)} \right|^2 + 2 \left| \mathcal{A}_{n+1,\ell}^{(-)} \right| \left| \mathcal{A}_{n-1,\ell}^{(+)} \right| \cos[2\omega_{IR}\tau - \Delta\phi] \right)$$

and the asymmetry parameters β_k are define as follows:

$$\beta_k = \frac{1}{\mathcal{P}_n} \sum_{\ell=0,2} \sum_{\ell'=0,2} i^{\ell-\ell'} \sqrt{2\ell+1} \sqrt{2\ell'+1} \mathcal{A}_{\ell}^* \mathcal{A}_{\ell'} C_{\ell 0, \ell' 0}^{k0} C_{\ell 0, \ell' 0}^{k0}, \quad (5.10)$$

$C_{\ell 0, \ell' 0}^{k0}$ and $C_{\ell 0, \ell' 0}^{k0}$ are the Clebsch-Gordan coefficients.

The 2ω in the total probability beating is that of the traditional RABBITT and is present because of the two two-photon transitions, one down from $n+1$ and up from $n-1$, which each carry a phase $\pm\omega_{IR}\tau$. We are interested in the beating in asymmetry, the probability of the electron leaving up or down:

$$\mathcal{P}_n^{up} - \mathcal{P}_n^{down} = \int_0^{2\pi} d\phi \int_0^{\pi/2} d\theta \sigma(\theta) - \int_0^{2\pi} d\phi \int_{\pi/2}^{\pi} d\theta \sigma(\theta). \quad (5.11)$$

Taking advantage of the parity of the Legendre polynomials:

$$P_1(x) = -P_1(-x), \quad P_2(x) = P_2(-x), \quad P_3(x) = -P_3(-x), \quad P_4(x) = P_4(-x)$$

only the odd terms survive,

$$\mathcal{P}_n^{up-down} = \mathcal{P}_n \left(\beta_1 - \frac{1}{4}\beta_3 \right) \quad (5.12)$$

$$\beta_1 \propto \Re \left[\mathcal{A}_{n,p}^* \mathcal{A}_{n\pm 1,s} + \mathcal{A}_{n,p}^* \mathcal{A}_{n\pm 1,d} \right] \quad \text{and} \quad \beta_3 \propto \Re \left[\mathcal{A}_{n,p}^* \mathcal{A}_{n\pm 1,d} \right], \quad (5.13)$$

which carry the ω_{IR} beating in the photoionization distribution asymmetry.

5.2 Scattering State and Pulse

Scattering State Projections

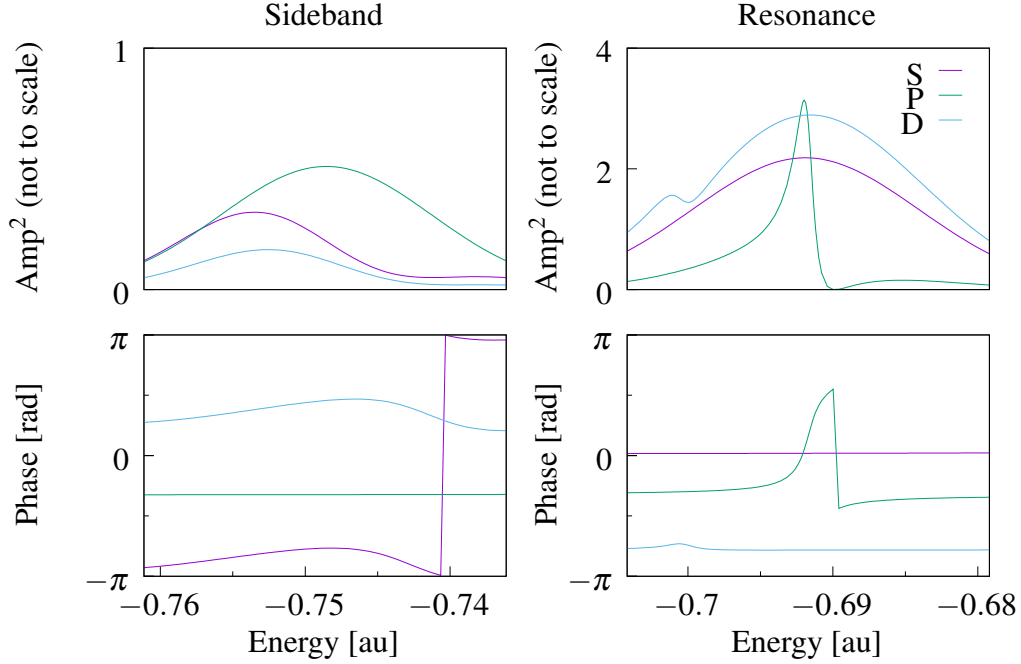


Figure 5.1: A plot of the wavefunction projected onto the S, P, and D scattering states after $\Delta t = 650$ au. The top row of plots are the amplitudes-squared, which are scaled dramatically for easier visibility, and the bottom row is the phase. Notice the phase increases by π at the resonant energy (~ -0.69 au) in the P symmetry.

Using an 10 cycle, 800 nm IR and two harmonics, $H_{38} = 2.1380$ au, $H_{39} = 2.1949$ au the system is excited into the $2s2p$ resonant state by absorbing one XUV photon or by absorbing one XUV photon plus one IR photon just as in the 1D model. Figure 5.1 displays the scattering amplitudes of the S, P, and D symmetries after the system (atom) is no longer interacting with the pulse. The P amplitude maintains a dramatic phaseshift typical of the $2s2p$ resonance. It is this phase our

technique will extract from experimental results, in particular, the asymmetry in the photoelectron distribution.

5.3 Photoionization

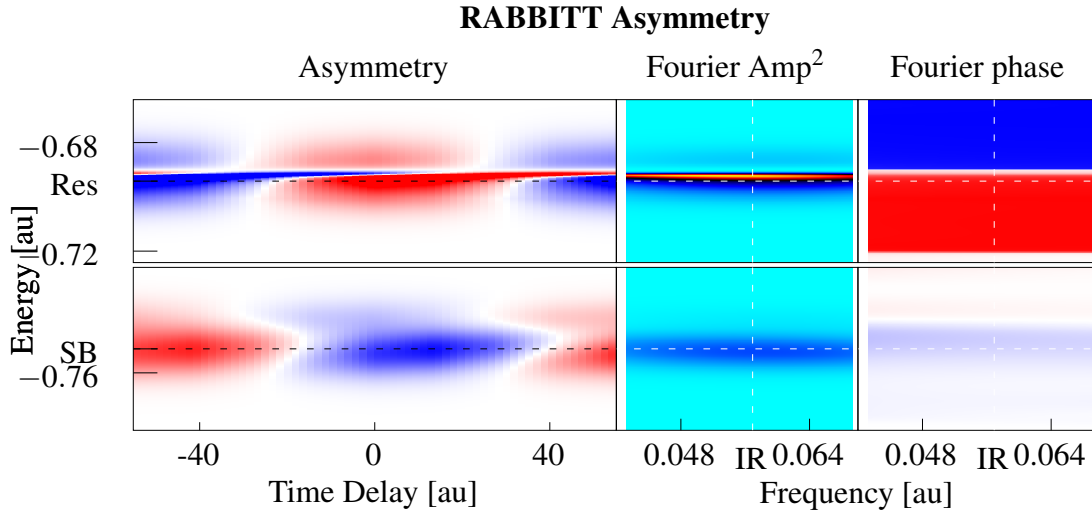


Figure 5.2: A plot of the asymmetry around the resonance $2s2p$ state ($E_{res} = -0.69$ au) and the sideband approximately $E_{sb} \sim -0.75$ au. The Fourier transform amplitude and phase is shown in the same regions. The phase varies between $-\pi$ (blue) and $+\pi$ (red).

Due to the interference between the S and D symmetries (even) with the P symmetry (odd) at the sideband and $2s2p$ resonance we can see the ω_{IR} beating in the amplitude of the asymmetry in figure 5.2. This parallels the results from the numerical model (figure 4.7) as expected and further verifies the validity of the 1D model as a tool to explore this phenomenon. There is a dramatic phaseshift as the energy (vertical axis) cross the $2s2p$ resonance of nearly π . The sideband also displays the phaseshift in the beating but it is modulated significantly by the emission of the IR-

photon due to the finite length of IR pulse. Following the recipe used before, the Fourier transform with respect to the delay of the IR pulse is calculated and the region near ω_{IR} is integrated and analyzed.

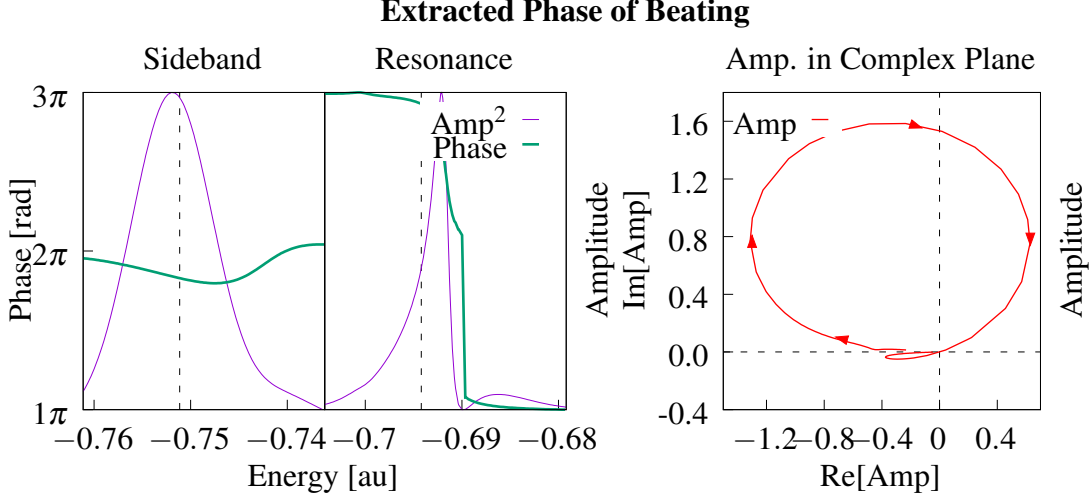


Figure 5.3: The extracted phaseshift at the sideband (left) and $2s2p$ resonance (middle) are shown on top of the respective square-amplitudes (not to scale). At the resonance, the phase jumps by π and when the amplitude crosses zero there is a discontinuity of π . The complex amplitude is plotted in the complex-plane on right. The discontinuity occurs as the amplitude crosses the origin.

In fact, the amplitude of the beating at the resonance maintains the typical Fano-resonance profile, occuring when a discrete state and a continuum state interfere [30]. This profile is characterized by three parameters, the quality parameter, q , which defines the asymmetry of the amplitude and Γ which defines the width of the resonance and the position of the resonance E_{res} . The resonance width defines the decay time of the resonance which is on the order of 10^{-3} au. The Fano resonance amplitude is expressed as follows:

$$\mathcal{A} \propto \frac{\varepsilon + q}{\varepsilon - i}, \quad \varepsilon = \frac{E - E_{res}}{\frac{\Gamma}{2}}. \quad (5.14)$$

where ε is the reduced energy, q is the resonance quality parameter and Γ is the resonance width parameter.

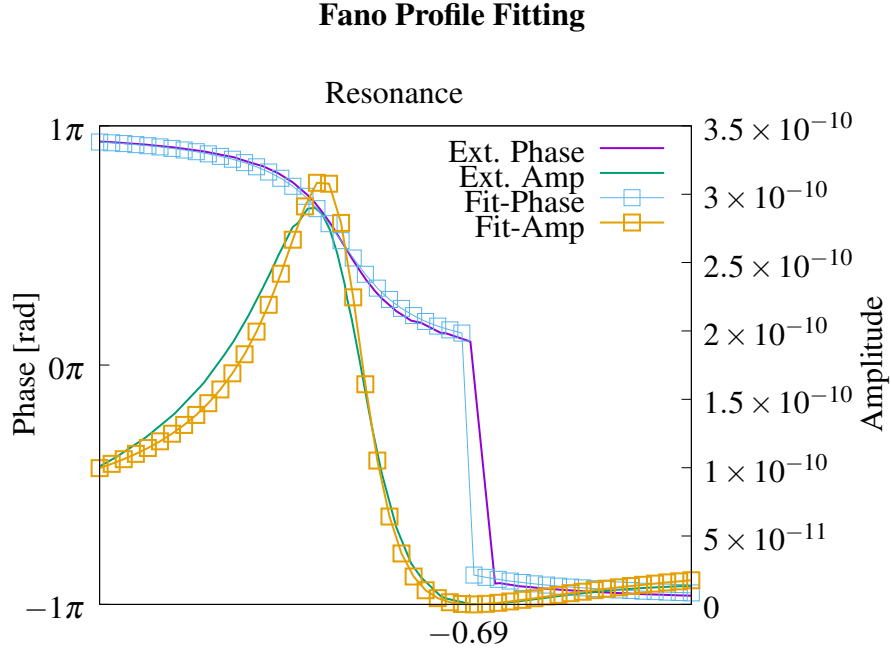


Figure 5.4: The complex amplitude is fit to the Fano profile expression 5.14. The resonance parameters found are: $q \approx -2.5$, $E_{res} \approx -0.691$ au and $\Gamma \approx 0.001418$ au

The complex amplitude of the beating is fit to the Fano expression in order to gather the parameters of the resonance. The quality parameter found is $q \approx -2.5$ and the width $\Gamma \approx 0.001418$ au and the resonance center at $E_{res} \approx -0.691$ au which compares well with the values taken from literature, $E_{res} = -0.69$ au, $q = -2.5$, $\Gamma = 0.00137$ au.

CHAPTER 6

CONCLUSION

In this thesis, we have presented a new interferometric spectroscopic technique, "Checkerboard RABBITT". The checkerboard RABBITT technique demonstrates the capability of reconstructing the phase information for resonant photoemission without the distortions associated with the traditional RABBITT approach. This is made possible by the addition of even harmonics into the attosecond pulse train and therefore the introduction of direct interference between one- and two-photon transition pathways. The distortion of the traditional RABBITT method, due to the absorption or emission of a photon of indeterminate energy from a pulse of finite duration, is able to simultaneously be quantified by the new approach. Another significant advantage of checkerboard RABBITT is the ability to measure even resonances, which the traditional scheme cannot. The only way to reach such a resonance in the traditional scheme would be at the sideband, where both pathways acquire the same phase which cancels and is invisible in the beating.

We have developed a one-dimensional model which provides a minimal system that demonstrates features that can be extended to arbitrary autoionizing states and captures the essence of the new technique. This model is investigated both analytically and numerically allowing the exploration to extend to helium, which confirms and mirrors the results of the one-dimensional model and has experimental consequence. In fact, there are already ongoing efforts of experimen-

tal collaborators to confirm the predictions of the calculations in helium. Using the checkerboard RABBITT technique developed in this thesis we are able to reconstruct the shape-resonances of the one-dimensional model and the Feshbach resonances of helium from the anisotropy of the photoemission.

Going forward, it is important to introduce all significant harmonics normally comprising an APT. The presence of multiple harmonics gives rise to an additional two-photon transition path to each associated photoelectron energy, which would require one to modify the reconstruction protocol. Exploration of the envelope effects would also provide valuable information when considering how to best implement this technique in experiment. For example, the duration of the infrared pulse can introduces variations in the amplitude of the beating in the on- or off-resonance bands. The addition of a resonance in the final state would allow for the examination of the radiative coupling between two resonances. Exploration into these possibilities is ongoing as well as the preparation of a paper based on these results.

APPENDIX A

SCATTERING STATE PHASES AND NORMALIZATION

Wavefunctions:

$$\psi_o(x) = A_o(k) \sin(kx + \phi_o(k)) \quad \text{Odd states} \quad (\text{A.1})$$

$$\psi_e(x) = A_e(k) \sin(kx + \phi_e(k)) \quad \text{Even states.} \quad (\text{A.2})$$

For the odd wavefunctions the phase in region II and region III must be zero:

$$\phi_o^{II}(k) = \phi_o^{III}(k) = 0 \quad \text{Must be true for odd wavefunctions.}$$

The phase in region IV can be found using the boundary conditions from Eq. (3.1) and Eq. (3.2).

$$\begin{aligned} \psi(x)|_{x=x_0^+} &= \psi(x)|_{x=x_0^-} \\ \psi'(x)|_{x=x_0^+} &= \psi'(x)|_{x=x_0^-} \pm 2\alpha \psi(x)|_{x=x_0}. \end{aligned}$$

Where $x_0 = a$, and $\pm\alpha = +V_+$:

$$A_o^{IV}(k) \sin(ka + \phi_o^{IV}(k)) = A_o^{III}(k) \sin(ka) \quad (\text{A.3})$$

$$A_o^{IV}(k) \cos(ka + \phi_o^{IV}(k)) = A_o^{III}(k) \cos(ka) + \frac{2V_+}{k} A_o^{III}(k) \sin(ka). \quad (\text{A.4})$$

Then we divide Eq. (A.4) by Eq. (A.3) and solve for $\phi_o^{IV}(k)$:

$$\cot(ka + \phi_o^{IV}(k)) = \cot(ka) + \frac{2V_+}{k} \quad (\text{A.5})$$

$$\phi_o^{IV}(k) = \text{arccot} \left(\cot(ka) + \frac{2V_+}{k} \right) - ka \quad (\text{A.6})$$

For the even phase the phase in region II/III is nonzero but opposite:

$$\phi_e^H(k) = -\phi_e^{III}(k) \quad (\text{A.7})$$

Again using the boundary conditions at $x_0 = 0$ and $\pm\alpha = -V_-$:

$$A_e^{III}(k) \sin(\phi_e^{III}(k)) = A_e^H(k) \sin(\phi_e^H(k)) \quad (\text{A.8})$$

$$A_e^{III}(k) \cos(\phi_e^{III}(k)) = A_e^H(k) \cos(\phi_e^H(k)) - \frac{2V_-}{k} A_e^H(k) \sin(\phi_e^H(k)) \quad (\text{A.9})$$

Once again we divide Eq. (A.9) by Eq. (A.8) and using Eq. (A.7) solve for $\phi_e^{III}(k)$.

$$\begin{aligned} \cot(\phi_e^{III}(k)) &= \cot(\phi_e^H(k)) - \frac{2V_-}{k} \\ \cot(\phi_e^{III}(k)) &= -\cot(\phi_e^{III}(k)) - \frac{2V_-}{k} \\ \cot(\phi_e^{III}(k)) &= -\frac{V_-}{k} \\ \tan(\phi_e^{III}(k)) &= -\frac{k}{V_-} \\ \phi_e^{III}(k) &= -\arctan \left(\frac{V_-}{k} \right) \end{aligned} \quad (\text{A.10})$$

Finally, to solve for $\phi_e^{IV}(k)$ we apply the boundary conditions at $x_0 = a$ and $\pm\alpha = +V_+$:

$$A_e^{IV}(k) \sin(ka + \phi_e^{IV}(k)) = A_e^{III}(k) \sin(ka + \phi_e^{III}(k)) \quad (\text{A.11})$$

$$A_e^{IV}(k) \cos(ka + \phi_e^{IV}(k)) = A_e^{III}(k) \cos(ka + \phi_e^{III}(k)) - \frac{2V_-}{k} A_e^{III}(k) \sin(ka + \phi_e^{III}(k)) \quad (\text{A.12})$$

and as before we divide the equations and solve for $\phi_e^{IV}(k)$.

$$\begin{aligned} \cot(ka + \phi_e^{IV}(k)) &= \cot(ka + \phi_e^{III}(k)) + \frac{2V_+}{k} \\ \phi_e^{IV}(k) &= \text{arccot} \left(\cot(ka + \phi_e^{III}(k)) + \frac{2V_+}{k} \right) - ka \end{aligned} \quad (\text{A.13})$$

For the normalization constants we first choose to normalize the interior to one, $A_e^{II} = A_e^{III} = 1$ and $A_o^{II} = A_o^{III} = 1$. Then we apply the boundary conditions at $x_0 = a$ but square then sum them.

For example the odd normalization:

$$\begin{aligned} (A_o^{IV}(k))^2 \sin^2(ka + \phi_o^{IV}(k)) &= \sin^2(ka) \\ (A_o^{IV}(k))^2 \cos^2(ka + \phi_o^{IV}(k)) &= \left(\cos(ka) + \frac{2V_+}{k} \sin(ka) \right)^2. \end{aligned}$$

And summed:

$$(A_o^{IV}(k))^2 (\sin^2(ka + \phi_o^{IV}(k)) + \cos^2(ka + \phi_o^{IV}(k))) = \sin^2(ka) + \left(\cos(ka) + \frac{2V_+}{k} \sin(ka) \right)^2.$$

$$(A_o^{IV}(k))^2 = 1 + \left(\frac{2V_+}{k} \sin(ka) \right)^2 + 2 \frac{2V_+}{k} \sin(ka) \cos(ka) \quad (\text{A.14})$$

$$A_o^{IV}(k) = \sqrt{1 + \left(\frac{2V_+}{k} \sin(ka) \right)^2 + \frac{2V_+}{k} \sin(2ka)}. \quad (\text{A.15})$$

The same process for the even states yields:

$$\begin{aligned} (A_e^{IV}(k))^2 \sin^2(ka + \phi_e^{IV}(k)) &= \sin^2(ka + \phi_e^{III}(k)) \\ (A_e^{IV}(k))^2 \cos^2(ka + \phi_e^{IV}(k)) &= \left(\cos(ka + \phi_e^{III}(k)) + \frac{2V_+}{k} \sin(ka + \phi_e^{III}(k)) \right)^2. \end{aligned}$$

And summed:

$$(A_e^{IV}(k))^2 = \sin^2(ka + \phi_e^{III}(k)) + \left(\cos(ka + \phi_e^{III}(k)) + \frac{2V_+}{k} \sin(ka + \phi_e^{III}(k)) \right)^2.$$

$$(A_e^{IV}(k))^2 = 1 + \left(\frac{2V_+}{k} \sin(ka + \phi_e^{III}(k)) \right)^2 + 2 \frac{2V_+}{k} \sin(ka + \phi_e^{III}(k)) \cos(ka + \phi_e^{III}(k)) \quad (\text{A.16})$$

$$A_e^{IV}(k) = \sqrt{1 + \left(\frac{2V_+}{k} \sin(ka + \phi_e^{III}(k)) \right)^2 + \frac{2V_+}{k} \sin(2ka + 2\phi_e^{III}(k))}. \quad (\text{A.17})$$

LIST OF REFERENCES

- [1] S. R. Leone et al., “What will it take to observe processes in ‘real time’?”, *Nat. Photonics* **8**, 162 (2014).
- [2] M. Hentschel et al., “Attosecond metrology.”, *Nature* **414**, 509 (2001).
- [3] G. Sansone et al., “Isolated Single-Cycle Attosecond Pulses”, *Science* **314**, 443 (2006).
- [4] F. Krausz and M. Ivanov, “Attosecond physics”, *Rev. Mod. Phys.* **81**, 163 (2009).
- [5] H. G. Muller, “Reconstruction of attosecond harmonic beating by interference of two-photon transitions”, *Appl. Phys. B-Lasers O.* **74**, 17 (2002).
- [6] P. Agostini and L. F. DiMauro, “The physics of attosecond light pulses”, *Rep. Prog. Phys.* **67**, 1563 (2004).
- [7] P. M. Paul, “Observation of a Train of Attosecond Pulses from High Harmonic Generation”, *Science* **292**, 1689 (2001).
- [8] A. L’Huillier and P. Balcou, “High-order harmonic generation in rare gases with a 1-ps 1053-nm laser”, *Phys. Rev. Lett.* **70**, 774 (1993).
- [9] P. B. Corkum, “Plasma perspective on strong field multiphoton ionization”, *Phys. Rev. Lett.* **71**, 1994 (1993).

- [10] R. López-Martens et al., “Amplitude and phase control of attosecond light pulses”, Phys. Rev. Lett. **94**, 1 (2005).
- [11] G. Laurent et al., “Attosecond control of orbital parity mix interferences and the relative phase of even and odd harmonics in an attosecond pulse train”, Phys. Rev. Lett. **109**, 083001 (2012).
- [12] J. Mauritsson et al., “Coherent electron scattering captured by an attosecond quantum stroboscope”, Phys. Rev. Lett. **100**, 1 (2008).
- [13] T. T. Luu and H. J. Wörner, “Measurement of the berry curvature of solids using high-harmonic spectroscopy”, Nat. Commun. **9**, 916 (2018).
- [14] T. J. Hammond et al., “Integrating solids and gases for attosecond pulse generation”, Nat. Photonics **11**, Article, 594 (2017).
- [15] Y. S. You et al., “High-harmonic generation in amorphous solids”, Nat. Commun. **8**, 724 (2017).
- [16] V. Vénier, R. Taïeb, and A. Maquet, “Phase dependence of (n+1)-color (n>1) ir-uv photoionization of atoms with higher harmonics”, Phys. Rev. A **54**, 721 (1996).
- [17] Á. Jiménez Galán, L. Argenti, and F. Martín, “Modulation of Attosecond Beating in Resonant Two-Photon Ionization”, Phys. Rev. Lett. **113**, 263001 (2014).
- [18] D. Pile, “X-rays: Bottle spectrometer”, Nat. Photonics **10**, 2 (2015).
- [19] A. Kothe et al., “Time-of-flight electron spectrometer for a broad range of kinetic energies”, Rev. Sci. Instrum. **84**, 1 (2013).

- [20] R. B. Opsal, K. G. Owens, and J. P. Reilly, “Resolution in the linear time of flight mass spectrometer”, *Anal. Chem.* **57**, 1884 (1985).
- [21] N. G. Kling et al., “Thick-lens velocity-map imaging spectrometer with high resolution for high-energy charged particles”, *J. Instrum.* **9**, P05005 (2014).
- [22] A. R. Bainbridge and W. A. Bryan, “Velocity map imaging of femtosecond laser induced photoelectron emission from metal nanotips”, *New J. Phys.* **16**, 103031 (2014).
- [23] J. Ullrich et al., “Recoil-ion and electron momentum spectroscopy: reaction-microscopes”, *Rep. Prog. Phys.* **66**, 1463 (2003).
- [24] R. Dörner et al., “Cold Target Recoil Ion Momentum Spectroscopy: A ’momentum microscope’ to view atomic collision dynamics”, *Phys. Rep.* **330**, 95 (2000).
- [25] L. Argenti et al., “Control of photoemission delay in resonant two-photon transitions”, *Phys. Rev. A* **95**, 1 (2017).
- [26] B. Johnson, “New numerical methods applied to solving the one-dimensional eigenvalue problem”, *J. Chem. Phys.* **67**, 4086 (1977).
- [27] B. Johnson, “The renormalized numerov method applied to calculating bound states of the coupled-channel schroedinger equation”, *J. Chem. Phys.* **69**, 4678 (1978).
- [28] S. D. Conte and C. W. D. Boor, *Elementary numerical analysis: an algorithmic approach*, 3rd Edition (McGraw-Hill Higher Education, 1980).
- [29] H. Bachau, E. Cormier, P. Decleva, J. E. Hansen, and F. Martín, “Applications of b -splines in atomic and molecular physics”, *Rep. Prog. Phys.* **64**, 1815 (2001).

- [30] U. Fano, “Effects of configuration interaction on intensities and phase shifts”, Phys. Rev. **124**, 1866 (1961).